DIMITRI Algorithm Theoretical Basis Document [03]

Interband Vicarious Calibration over Sunglint

ARGANS

ESA contract: 4000106294

ARGANS Reference: 003-013: MO-SCI-ARG-TN-004c

Date: 28th May 2014

Version: 1.0

Authors

NAME	AFFILIATION	CONTACT
K. Barker	ARGANS Ltd, UK	kbarker@argans.co.uk
D. Marrable	ARGANS Ltd, UK	dmarrable@argans.co.uk
J. Hedley	ECS Ltd, UK	j.d.hedley@envirocs.com
C. Mazeran	Solvo, France	constant.mazeran@solvo.fr

Acknowledgements

The Siro modelling included in Figure 5 and Figure 6 were produced Jukka Kujanpää of the Finnish Meteorological Institute in the context of the ESA project 'GEO-HR' AO/1-7084/12/NL/AF, and are reproduced from Hedley *et al*. (2013).

TABLE OF CONTENTS

List of Figures

List of Tables

1 Introduction

1.1 Scope of this ATBD

Under ESA contract 4000106294 ("Earth Observation Multi-Mission Phase-E2 Operational Calibration: assessment of enhanced and new methodologies, technical procedures and system scenarios") DIMITRI v2.0 has been developed further and is now available as DIMITRI v3.0, in which new methodologies have been included, and the automated cloud screening improved.

An ATBD describes each of the new developments. The set of three ATBDs are:

[01] Automated Cloud Screening DIMITRI v3.0

[02] Absolute vicarious calibration over Rayleigh Scattering

[03] Vicarious calibration over Sunglint

This ATBD document is concerned with describing the vicarious calibration over sunglint. The document:

1) Describes the principles of this method;
2) Describes the implementation in DIMITRI v3.0 making use of LibradTran LUTs;
3) Presents results of implementation, sensitivity analyses and uncertainty estimations;
4) Describes the updates made to DIMITRI Human Machine Interface (HMI) and how the user can use this methodology.

1.2 DIMITRI

The Database for Imaging Multi-Spectral Instruments and Tools for Radiometric Intercomparison (DIMITRI) is an open-source software giving gives users the capability of long term monitoring of instruments for systematic biases and calibration drift, with a database of L1b top of atmosphere radiance and reflectances from a number of optical medium resolution sensors.

DIMITRI comes with a suite of tools for comparison of the L1b radiance and reflectance values originating from various medium resolution sensors over a number of radiometrically homogenous and stable sites (Table 1) at TOA level, within the 400nm – 4µm wavelength range. The date range currently available is 2002 to 2012. DIMITRI's interface enables radiometric intercomparisons based on user-selection of a reference sensor, against which other sensors are compared. DIMITRI contains site reflectance averages and standard deviation (and number of valid pixels in the defined region of interest, or ROI), viewing and solar geometries and auxiliary and meteorology information where available; this allows extractions of windspeed and direction, surface pressure, humidity and ozone concentration from MERIS products, and water vapour and ozone concentration from VGT-2 products. Each observation is automatically assessed for cloud cover using a variety of different automated algorithms depending on the radiometric wavelengths available; manual cloud screening is also visually performed using product quicklooks to flag misclassified observations. DIMITRI also provides a platform for radiometric intercalibration from User defined matching parameters: geometric, temporal, cloud and ROI coverage. Other capabilities and functions include: product reader and data extraction routines, radiometric recalibration & bidirectional reflectance distribution function (BRDF) modelling, quicklook generation with ROI overlays, instrument spectral response comparison tool, VEGETATION simulation.

DIMITRI v2.0 has these two methodologies:

1. **Radiometric intercomparison based on angular and temporal matching**, based on the methodology of Bouvet (2006) and Bouvet *et al* (2007): Concomitant observations made under similar geometry and within a defined temporal window are intercompared at similar spectral bands.
2. **Radiometric intercomparison of VEGETATION simulated and actual observations**, making use of the ability to combine timeseries from all sensors into one "super sensor" and fitting a 3-parameter BRDF model to all observations to simulate TOA spectra of VEGETATION-2 (Bouvet, 2011).

DIMITRI v3.0 is evolved from DIMITRI v2.0 and has two additional methodologies and an improved automated cloud screening and cloud screening tool:

1. **Absolute vicarious calibration over Rayleigh Scattering,** based on the methodology of Hagolle *et al* (1999) and Vermote *et al* (1992) and utilising open ocean observations, to simulate molecular scattering (Rayleigh) in the visible and comparing against *the observed* ρ_{toa} to derive a calibration gain coefficient;
2. **Vicarious calibration over sunglint**, based on the methodology of Hagolle *et al* (2004); similar to Rayleigh scattering approach but accounting for sunglint reflectance contribution;
3. **Improved automated cloud screening,** exploiting the spatial homogeneity (smoothness) of validation sites when cloud free and applying a statistical approach utilising σ (ρ_{toa}) over a ROI, and defining variability thresholds, such as dependence on wavelength and surface type.

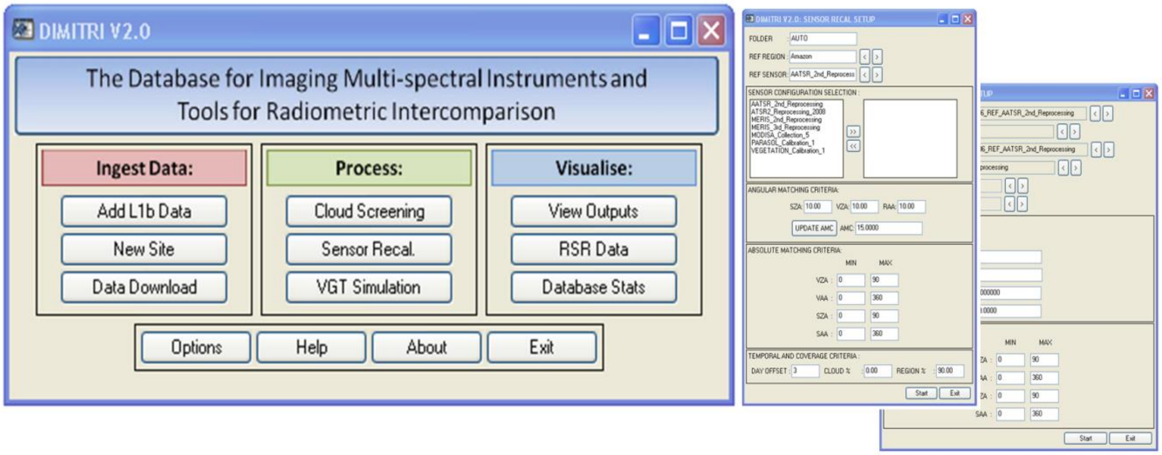

Figure 1: DIMITRI v2.0 screenshot

Table 1: Sensors and sites included in the DIMITRI v2.0 database

SENSOR	SUPPLIER
AATSR (Envisat)	ESA
MERIS, 2nd and 3rd reprocessing (Envisat)	ESA
ATSR-2 (ERS-2)	ESA
MODIS-A (Aqua)	NASA
POLDER-3 (Parasol)	CNES
VEGETATION-2 (SPOT5)	VITO

SITE	SITE TYPE
Salar de Uyuni, Bolivia	Salt lake
Libya-4, Libyan Desert	Desert
Dome-Concordia (Dome-C), Antarctica	Snow
Tuz Golu, Turkey	Salt Lake
Amazon Forest	Vegetation
BOUSSOLE, Mediterranean Sea	Marine
South Pacific Gyre (SPG)	Marine
Southern Indian Ocean (SIO)	Marine

DIMITRI_v2.0 and v3.0 are freely (without L1b data) available. DIMITRI_v2.0 is available following registration at www.argans.co.uk/dimitri. DIMITRI_v3.0 is a larger file (approx. 55GB) so is available upon request; ARGANS or ESA will make it available on an FTP server site.

2 Interband Vicarious Calibration over Sunglint

2.1 Overview

Interband calibration for Near Infra-red (NIR) and Shortwave Infrared (SWIR) bands can be computed by utilising the flat spectral slope of sun glint; the TOA reflectance can be simulated (e.g. Figure 2), similarly to the Rayleigh calibration methodology but taking into account the sunglint reflectance contribution. The magnitude of the sunglint reflectance is mainly dependent on the viewing and solar geometries and surface roughness (i.e. wind speed; Hagolle *et al*., 2004). A 'calibration' band (usually around 560 nm) is used to extrapolate the sunglint reflectance into the NIR/SWIR bands for comparison against the observed values. Pixels within the defined ROI are now selected only if they fall within a defined cone of specular reflection; as the sunglint reflectance is spectrally flat (in the NIR/SWIR) clouds will be detected if the ratio between two user defined bands is less than a defined threshold. This cloud screening methodology was shown to successfully classify pixels by Hagolle *et al*. (2004).

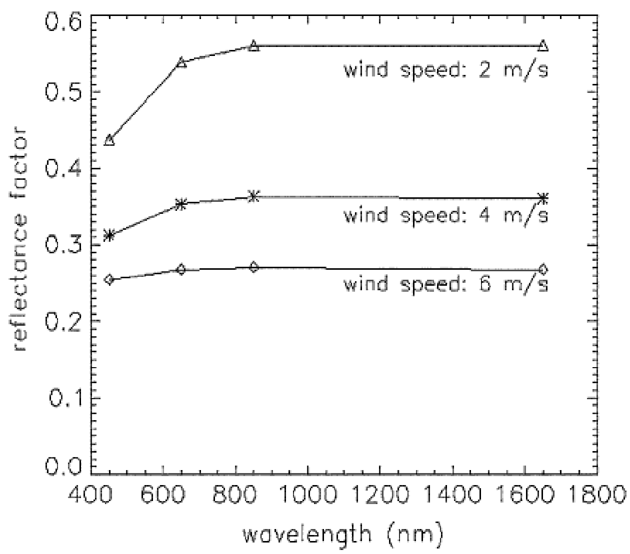

Figure 2: Example of TOA reflectance factors simulated in a viewing direction (solar zenith = 40, viewing zenith = 43.5, relative azimuth = 174) close to the exact specular direction, for all VEGETATION spectral bands and for three different values of wind speed (Hagolle *et al*., 2004).

The sunglint method is often used together with Rayleigh method, see e.g., Nicolas *et al*. (2006) who apply it to Seviri. Sunglint (the Fresnel reflection of sunlight on the air-sea interface) can be used as a spectrally flat target to calibrate one spectral band according to another. In Nicolas *et al*. (2006), the visible (VIS) 0.6 band was used as a reference, after adjustment from Rayleigh scattering method, and cross-calibrate the VIS 0.8 and NIR 1.6 bands. The sunglint signal ranged from 10 to 40 % of maximum dynamic for each of the three bands.

Závody *et al*. (1998) provide details of their implementation of sunglint calibration method applied to calibration of ATSR-2 1.6-µm channel using simultaneous measurements made in the 3.7-µm channel in Sun Glint. The theoretical model for their calibration is described in the following steps:

- finding the increase in radiance at 3.7 mm caused by sun glint,
- characterizing the atmosphere in the glint region,
- computing the effective reflectivity of the sea surface at 3.7 mm,
- finding the 1.6-mm surface reflectivity,
- calculating the 1.6-mm calibration coefficient.

Hagolle *et al*. (2004) conclude that despite the drawback of relying on the absolute calibration of a reference spectral band, this is one of the rare methods that can provide accurate calibration results for near-infrared spectral bands up to 1650 nm, without requiring costly in situ measurements simultaneously to the satellite overpass. The paper details the sunglint calibration method and its error budget, and gives the results obtained with the VEGETATION-2 instrument. The sunglint calibration method compares the measurements provided by VEGETATION-2 above sunglint, to an estimation of the top-of-atmosphere reflectance. The authors have evaluated error budget showing that if the reference spectral band uncertainty is below 3% (3 sigma), the calibration of NIR bands can be obtained with an uncertainty below 4% (3 sigma) at 850 nm and below 5% at 1650 nm (3 sigma). Apart from the reference spectral band calibration uncertainty, the main error contributors are the uncertainty on the water refraction index at 1650 nm, and the aerosol properties variability.

2.2 Algorithm description

The implemented DIMITRI sun glint calibration is based on the methodologies described in Hagolle *et al* (1999; 2004) and Nicolas *et al* (2006) and uses the specular reflection of the sun (i.e. sun glint) on the sea surface to transfer calibration of 565 nm (or close) band to the NIR bands (670 nm and above, relevant to each to sensor).

2.2.1 Oceanic sites

Sun glint calibration is applicable on stable oceanic regions, with low concentration of phytoplankton and sediment to have little impact of the marine signal in the red and near-infrared bands, and far from land to ensure purely maritime aerosol model. Two regions in DIMITRI are candidates: South Pacific Gyre (SPG) and South Indian Ocean (SIO).

2.2.2 Data screening

Clear conditions must be chosen to avoid any signal contamination by clouds, haze or cloud shadows.

A low wind speed is required for both ensuring no presence of whitecaps; typically it is limited to 5 m/s.

In order to select only pixels impacted by the sunglint, the viewing direction must be within a cone around the specular direction. For a flat sea surface, the angle between viewing direction and specular direction is given by the backscattering angle:

$$\cos\theta_g = \cos\theta_s \cos\theta_v - \sin\theta_s \sin\theta_v \cos\Delta\varphi \quad (1)$$

Where θ_s, θ_v and $\Delta\varphi$ are respectively the sun zenith angle, view zenith angle and relative azimuth angle. To take into account wavy surface, a cone around θ_g=0° is allowed, for instance of about 15° (default value proposed in DIMITRI).

Contrary to Hagolle *et al*. (1999) using PARASOL off-glint data, DIMITRI database contains a large set of sensors without directional capability (e.g. MERIS, MODIS). This precludes computing the aerosol optical thickness from the radiometry. Therefore, as presented hereafter, a climatological value must be given by user for all measurements; default value proposed at 865 nm is 0.02, corresponding to Rayleigh scattering retrieval out of glint over SPG and SIO, as described in Barker *et al* (2013). A test is conducted a-posteriori on the retrieved optical at 865 nm, after glint estimate: data are screened with a threshold of 0.02 between the climatological value and this retrieved estimate, so that only consistent inversions are kept.

2.2.3 Marine model

DIMITRI marine model follows Morel and Maritorena (2001), which is an update of Morel (1988) used in Hagolle *et al*. (1999). It provides an estimate of irradiance reflectance at null depth, R(0^-) , from 350 to 700 nm, as a function of chlorophyll concentration and sun zenith angle. The water absorption coefficients of pure water are derived from Pope and Fry (2007) and Kou *et al*. (1993) and scattering coefficients from Table 1 of Smith and Baker (1981).

An excellent agreement is found between the original Morel and Maritorena (2001) model and DIMITRI implementation over the 400-700 nm spectral range, see Figure 3; discrepancy for wavelengths shorter than 400 nm, not considered in the vicarious calibration, are due to slight differences in input water coefficients.

Conversion from R(0^-) to marine reflectance above sea surface is given by Morel and Gentili (1996):

$$\rho_w(\lambda) = \pi \frac{\Re}{Q} R(0^-) \tag{2}$$

Where:

$\Re$ is the term accounting for all the reflection and refraction effects, with averaged value of 0.5287 for moderate wind speed (see Appendix D of Morel and Gentili, 1996); and

Q is the ratio of irradiance to radiance (at 0^-); without further details available in the Hagolle *et al*. (1999) methodology we consider here Q= π for isotropic distribution.

Note that there is no need for foam modelling since the vicarious calibration methodology only selects low wind speed modulus.

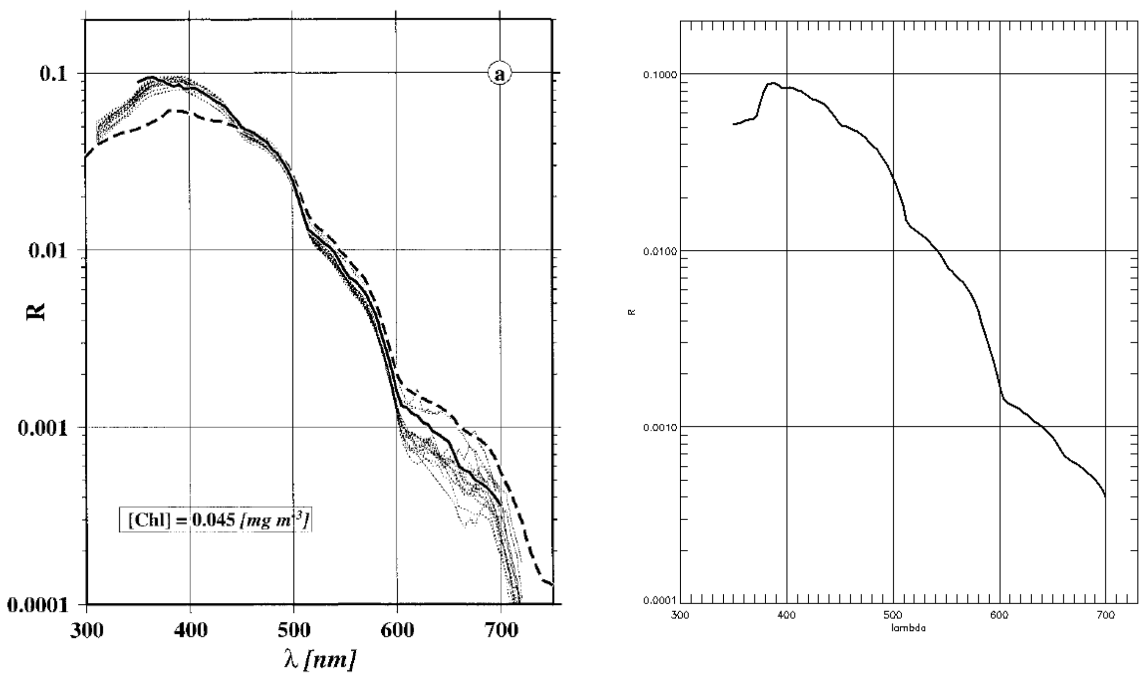

Figure 3: Comparison of irradiance reflectance spectrum between Morel and Maritorena (2001) (left, their figure 10a, solid thick line) and DIMITRI model (right) for a chlorophyll concentration of 0.045 mg/m3.

2.2.4 Atmospheric model

The total TOA signal can be written as

$$\rho_{TOA}(\lambda) = t_{gas}(\lambda)\big(\rho_{path}(\lambda) + t_{down}(\lambda) * t_{up}(\lambda) * \rho_w(\lambda) + T_{down}(\lambda) * T_{up}(\lambda)\rho_G\big) \quad (3)$$

Where:

t_{gas} is the transmittance (downward and upward) due to absorbing gas as O3, O2 and H2O

ρ_{path} is the atmospheric reflectance due to Rayleigh and aerosols and their multiple-scattering interaction

t_{down} and t_{up} are respectively the downward and upward total transmittance (i.e. direct + diffuse) due to Rayleigh and aerosol

ρ_w is the marine signal already described

T_{down} and T_{up} are the downward and upward direct transmittances

ρ_G is the sun glint reflectance at sea level.

The calibrated bands in the visible are only impacted by ozone. Hence the gaseous transmittance is computed by Beer's law:

$$t_{O_3}(\lambda) = e^{-\tau_{O_3}(\lambda) * O_3 * M} \quad (4)$$

Where:

O_3 is the ozone concentration of actual measurement

τ_{O_3} the ozone optical thickness at a standard concentration (already provided in DIMITRI auxiliary data)

M the air mass fraction.

In the near-infra red, the impact of water vapour is lower than 0.2% at 865 nm and less at other bands expect 709 nm. The impact of O_2 is of about 0.1% at 779 nm. Because DIMITRI currently does not contains auxiliary data about those gases, their transmittance is assumed to be unity (this will be included in error budget), and absorption bands (like 708 nm, 761 nm, 900 nm) are excluded of the vicarious calibration by a array of indices common to all DIMITRI wavelengths

The sun glint reflectance ρ_G is taken from the isotropic model of Cox and Munk (1954) as a function of wind speed modulus and geometry:

$$\rho_G = CM54(w_m, \theta_s, \theta_v, \Delta\varphi, \lambda) \tag{5}$$

The spectral dependence is due to the Fresnel coefficient, computed as a function of water refraction index; for a salinity of 35 PSU and temperature of 12°C the spectral variation of this index yields to a variation in the Fresnel coefficient (hence in the glint reflectance) of -2% from 560 to 865 nm, which is worth to taking into account.

Direct transmittance can be approximated by:

$$T_{down}(\lambda) * T_{up}(\lambda) = e^{-\left(\tau_R(\lambda)\frac{P}{P_{std}}+\tau_a(\lambda)\right)*M} \tag{6}$$

With τ_R being the Rayleigh optical thickness at standard pressure P_{std}, given by Hansen and Travis (1974) at any wavelength, P the actual pressure and τ_a the aerosol optical thickness, assumed to be known at a reference band (865 nm).

The path reflectance and total transmittance are computed by radiative transfer simulations (see hereafter) for a set of aerosol models and optical thicknesses, and stored in Look-up tables (LUT). Aerosols models must be representative of the calibration zone; marine models of Shettle and Fenn (1974) are here chosen for several relative humidities. Other more complex models may also be used for sensitivity study.

Retrieval of aerosol optical thickness from knowledge of the path reflectance follows the standard approach in ocean colour consisting in fitting the signal by a 2nd order polynomial in optical thickness, for every grid node of the simulation ($w_m, \theta_s, \theta_v, \Delta\varphi$); more particularly, the ratio of the path signal by the pure Rayleigh is used in fit as being found more robust (Antoine and Morel 1999):

$$\tau_a(\lambda) \rightarrow \left\{\frac{\rho_{path}}{\rho_R}\right\}(\lambda, \tau_a, w_m, \theta_s, \theta_v, \Delta\varphi) = XC_0 + XC_1\tau_a + XC_2(\tau_a)^2 \tag{7}$$

Where XC_i are the coefficients of the polynomial fit, defined for every wavelength, grid node and aerosol model.

Radiative transfer simulations are only tabulated for the unique standard atmospheric pressure. Because the actual measurements are under different pressures, P, generally systematically higher due to clear sky condition, a correction on ρ_{path} and $t_{down} * t_{up}$ is necessary. We follow here the MERIS pressure correction written in terms of:

$$\frac{\Delta P}{P_{std}} = \frac{(P - P_{std})}{P_{std}} \tag{8}$$

For ρ_{path}, Antoine and Morel (2011) proposes the following correction allowing to retrieve the exact signal within 0.5%

$$\rho_{path}(\lambda)_{|P} = \rho_{path}(\lambda)_{|P_{std}} * \left(1 + \frac{\Delta P}{P_{std}} \eta(\lambda)\right) \tag{9}$$

Where η is the contribution of molecules to total optical thickness:

$$\eta(\lambda) = \frac{\tau_R(\lambda)}{\tau_R(\lambda) + \tau_a(\lambda)} \tag{10}$$

Without this correction the error would be roughly similar as $\frac{\Delta P}{P_{std}}$ for low aerosol optical thickness, e.g. of 1% when $P = 1023$ hPa. It is worth noting that in the present work, the impact of pressure on computed ρ_{path} is lower because of combined use of a reference band and a calibrated band; the principle of this cancelation effect is detailed in Barker *et al.* (2013) for the Rayleigh scattering methodology (it is not strictly applicable to present case due to different algorithm but equivalent). Yet having a much lower impact because of the close red/near-infrared bands, the correction for pressure is also implemented here for consistent atmospheric modelling in both calibration methodologies.

For the total transmittance, the MERIS correction for pressure (see MERIS DPM, 2011) relies on the Rayleigh contribution of $t_R = e^{-\frac{1}{2}\tau_R * M}$, hence:

$$t_{down}(\lambda) * t_{up}(\lambda)_{|P} = t_{down}(\lambda) * t_{up}(\lambda)_{|P_{std}} * e^{-\frac{1}{2}\tau_R * M \frac{\Delta P}{P_{std}}} \tag{11}$$

2.2.5 Calibration coefficient algorithm

Glint calibration starts from a reference band λ_{ref} in the red assumed to be well-calibrated and intercalibrates other bands towards the near-infrared region. Hagolle *et al*. (1999) starts from

565 nm on PARASOL while Fougnie *et al*. (2012) uses 620 nm. The 665 nm band is also interesting for minimising ozone absorption, and can also be calibrated by the Rayleigh method. In DIMITRI this reference band is left to user choice. From a-priori knowledge of aerosol optical thickness τ_{865} and aerosol model, this reference band provides the sea surface state (i.e. wind speed) through Cox and Munk (1954). This model can be efficiently inversed alone by non-linear technique (here Newton method, at least when a solution exists), but we must consider that atmospheric path reflectance also depends in a lesser extent on wind speed. An iterative procedure is thus deployed to compute a wind speed that perfectly allows modelling the signal at reference band; three iterations are enough for converging on all cases encountered in DIMITRI, starting from the auxiliary wind speed. At the end of the algorithm, a check is done to inverse aerosol optical thickness and only pixels with sufficiently close value to the initial guess are kept.

The algorithm consists of following steps, repeated for all bands, λ:

1. Correct the TOA signal at λ_{ref} for ozone:

$$\rho_{TOA}^{oz}(\lambda_{ref}) = \rho_{TOA}(\lambda_{ref})/t_{O_3}(\lambda_{ref}) \tag{12}$$

2. Given a chlorophyll concentration, compute marine reflectance at band λ_{ref} following Morel and Maritorena (2001):

$$Chl, \theta_s \rightarrow \rho_w(\lambda_{ref}) \tag{13}$$

3. Propagate aerosol optical thickness τ_{865} at band λ_{ref} through tabulated spectral dependence for the given an aerosol model:

$$\tau_{865} \xrightarrow{LUT\ aer} \tau_a(\lambda_{ref}) \tag{14}$$

4. Compute Rayleigh optical thickness by Hansen and Travis (1974) and compute the direct transmittance:

$$T_{down}(\lambda_{ref}) * T_{up}(\lambda_{ref}) = e^{-\left(\tau_R(\lambda_{ref})\frac{P}{P_{std}}+\tau_a(\lambda_{ref})\right)*M} \tag{15}$$

5. Start loop for wind speed inversion:

5.1 Compute total path radiance (Rayleigh + aerosol) at band λ_{ref} and correct for pressure:

$$\tau_a(\lambda_{ref}) \xrightarrow{LUT\ aer} \rho_{path}(\lambda_{ref})_{|P_{std}} = \left\{\frac{\rho_{path}}{\rho_R}\right\}\left(\lambda_{ref}, \tau_{\lambda_{ref}}, w_m, \theta_s, \theta_v, \Delta\varphi\right) * \rho_R(\lambda_{ref}, w_m, \theta_s, \theta_v, \Delta\varphi) \quad (16)$$

$$\rho_{path}(\lambda_{ref})_{|P} = \rho_{path}(\lambda_{ref})_{|P_{std}} * \left(1 + \frac{\Delta P}{P_{std}} \eta(\lambda_{ref})\right) \quad (17)$$

5.2 Compute downward and upward total transmittances (direct + diffuse), accounting for Rayleigh and aerosol, at band λ_{ref}, and correct for pressure:

$$\tau_a(\lambda_{ref}) \xrightarrow{LUT\ aer} t_{down}(\lambda_{ref})_{|P_{std}} = \{t_{down}\}(\lambda_{ref}, \tau_\lambda, w_m, \theta_s) \quad (18)$$

$$\tau_a(\lambda_{ref}) \xrightarrow{LUT\ aer} t_{down}(\lambda_{ref})_{|P_{std}} = \{t_{up}\}(\lambda_{ref}, \tau_\lambda, \theta_v) \quad (19)$$

$$t_{down}(\lambda_{ref}) * t_{up}(\lambda_{ref})_{|P} = t_{down}(\lambda_{ref}) * t_{up}(\lambda_{ref})_{|P_{std}} * e^{-\frac{1}{2}\tau_R * M \frac{\Delta P}{P_{std}}} \quad (20)$$

5.3 Compute the glint reflectance:

$$\rho_G(\lambda_{ref}) = \frac{\rho_{TOA}^{oz}(\lambda_{ref}) - \rho_{path}(\lambda_{ref})_{|P} - t_{down}(\lambda_{ref}) * t_{up}(\lambda_{ref})_{|P} * \rho_w(\lambda_{ref})}{T_{down}(\lambda_{ref}) * T_{up}(\lambda_{ref})} \quad (21)$$

5.4 Inverse wind speed by Newton non-linear scheme:

Find w_m such that:

$$\rho_G(\lambda_{ref}) = CM54(w_m, \theta_s, \theta_v, \Delta\varphi, \lambda_{ref}) \quad (22)$$

6. Redo steps 1 to 4 at band λ with retrieved w_m and ρ_G and construct theoretical TOA signal:

$$\rho_{TOA}^{theo}(\lambda) = \rho_{path}(\lambda)_{|P} + t_{down}(\lambda) * t_{up}(\lambda)_{|\mathrm{P}} * \rho_w(\lambda) + T_{down}(\lambda) * T_{up}(\lambda)\rho_G \quad (23)$$

Where the spectral variation of $\rho_G(\lambda)$ is only due to Fresnel coefficient.

7. When λ=865 nm, estimate aerosol optical thickness by inversing the tabulated relationship:

$$\rho_{path}(865)_{|P} = \rho_{TOA}^{oz}(865) - t_{down}(865) * t_{up}(865)_{|\mathrm{P}} * \rho_w(865) - T_{down}(865) * T_{up}(865)\rho_G \quad (24)$$

$$\rho_{path}(865)_{|P_{std}} = \rho_{path}(865)_{|P}\left(1 - \frac{\Delta P}{P_{std}}\eta\left(865_{ref}\right)\right) \quad (25)$$

$$\frac{\rho_{path}(865)_{|P_{std}}}{\rho_R\left(865, w_m, \theta_s, \theta_v, \Delta\varphi\right)} \xrightarrow{LUT\ aer} \tau_a^{est}(865) \quad (26)$$

8. Keep only pixels consistent with the a priori known optical thickness:

$$|\tau_{865} - \tau_a^{est}(865)| \leq 0.02 \quad (27)$$

9. Eventually compute the glint intercalibration coefficient (relative toλ_{ref}) by:

$$A\left(\lambda\right) = \frac{\rho_{TOA}^{theo}\left(\lambda\right)}{\rho_{TOA}^{oz}\left(\lambda\right)} \quad (28)$$

In step 5.4, a first test must be to check that a solution does exist because the wind dependency of the Cox and Munk model is of the form:

$$CM54(w_m, \theta_s, \theta_v, \Delta\varphi) = \frac{A}{a + bw_m} e^{-\frac{B}{a + bw_m}} \quad (29)$$

With *a* and *b* being numerical constants (respectively 0.003 and0.00512) and *A* and *B* coefficients depending on $(\theta_s, \theta_v, \Delta\varphi)$ only, the maximum is reached at $\overline{w_m} = (B - a)/b$; hence if $\rho_G > CM54(\overline{w_m}, \theta_s, \theta_v, \Delta\varphi)$ no solution can be found by the Newton algorithm (it would converge to

$\overline{w_m}$ as an optimum but signal at λ_{ref} would not be consistent with the TOA modelling). In such a case, possibly corresponding to higher optical thickness than expected, pixels are discarded.

From step 6 it is important to include band $\lambda = \lambda_{ref}$ to check that $A(\lambda_{ref}) = 1$, meaning a perfect wind speed inversion.

It is worth noting that definition of $A(\lambda)$ in step 9 is the inverse of Rayleigh vicarious calibration coefficients, because it is relative to the λ_{ref} band, not to the absolute calibration of the sensor.

When this procedure is launched pixel-by-pixel, the calibration coefficient of a given observation is computed as the median on all associated pixels (median is found to be more robust than a simple mean).

The main differences with this method compared to the Hagolle *et al*. (1999) method are:

- The marine model is updated from Morel (1988) to Morel and Maritorena (2001);
- An aerosol contribution is used at λ_{ref}, as it impacts transmittances, hence the glint and wind speed estimates. A final test eventually removes all points that do not fit with the a priori value τ_{865}. In practice this value can be chosen as the mean of AOT found by the Rayleigh method on the same oceanographic zones.
- The AOT inversion follows the very same approach as the operational ocean colour data processing (Antoine and Morel 1999);
- The modelling of the path atmospheric signal is made directly using the RTM simulations as a function of optical thickness;
- The downward and upward transmittances include the aerosol contribution.

3 Uncertainty analysis

3.1 Published error budget

According to Hagolle *et al* (1999), the following are the main error sources for the methodology:

- Calibration error: error on the reference band induces error on the wind speed estimate. A 3% bias at 565nm introduces a 3% bias at 865 nm, hence no interband error. Error on 670 and 865 nm calibration would also impact aerosol detection, but this approach is not chosen and DIMITRI.
- Ozone: an uncertainty of 5% on ozone amount induces an error of less than 0.1%.
- Surface pressure: accurately known, it leads to 0.1%.
- Aerosol model: about 0.1%
- Chlorophyll: 0.3% error when the concentration is erroneous by 0.05 mg/m3 instead of 0.1 mg/m3; we understand it is implicitly for the 565 nm band, not in further red bands not impacted by chlorophyll in such oceanic regions.

This leads to a total published uncertainty of 1% maximum in interband calibration.

3.2 Sensitivity analysis on DIMITRI data

The main sources of uncertainty of the vicarious calibration are:

- The input parameters listed here above;
- The data screening condition, i.e. mainly clouds
- The pixel averaged on the calibration region.

Therefore a sensitivity analysis can be conducted with DIMITRI implementation to update the previously mentioned total error budget and to add new terms. We do not recompute uncertainty due to ozone and pressure as radiative transfer modellings are analogous between Hagolle *et al* (1999) and DIMITRI. Let us note that the published 0.1% uncertainty due to pressure is in line with our analysis and even an upper bound for calibrated bands close to the reference band (see Barker *et al* (2013) for details in the Rayleigh scattering methodology); we have also checked it directly by successively activating and de-activating the correction for pressure. In the following, the nominal run is a calibration of MERIS over SPG, with default options, in particular a MAR-99 aerosol model with 0.02 optical thickness at 865 nm (see section 4 for more details) and 665 nm as the reference band.

Sensitivity to cloud coverage: accepting 20% cloud coverage at ROI level, without considering pixel-by-pixel cloud mask, increases the number of calibration points from 10 to 15 and changes the median vicarious coefficients by 0.1% in the near-infrared bands; standard deviation of individual coefficients is unchanged. This is most probably due to similarity between glint and cloud signal at those bands (until 865 nm at least). We hence do not expect significant error when the 0% cloud coverage option is chosen, even if some clouds are not detected.

Sensitivity to aerosol model: switching to model MAR-70 or COAST-70 lead to a 0.1% error at all bands (consistent with Hagolle *et al*. (1999)) except at 885 nm for the COAST-70 model inducing a 0.3% change.

Sensitivity to aerosol optical thickness at 865 nm: changing the default value from 0.02 (assed on SPG time-series in off-glint conditions) to 0.08 (Hagolle *et al*. 2004) impact the calibration of 0.1%, except at 885 nm where it is of 0.3%.

Sensitivity to chlorophyll: replacing the chlorophyll monthly climatology by its extreme values (0.04 and 0.08 mg/m^3 over SPG) impacts the coefficients of 0.1%. This is a very good robustness compared to the Rayleigh vicarious calibration, obviously due to the considered bands in the red and near-infrared.

Sensitivity to sensor noise (pixel averaging): this can be assessed by comparing the DIMITRI output coefficient starting either from the averaged TOA signal, or from the pixel-by-pixel extraction (see section 3.3.3 about this processing mode). A first effect of using the averaged mode is to largely decrease the number of calibration points, from 10 to 3. The impact is around 0.1% or 0.2% depending on the bands.

Sensitivity to calibration of the reference band: we retrieve same number as Hagolle *et al*. (1999) until band 865 nm, i.e. a 3% calibration change roughly induces same change on the glint vicarious coefficients; the slight difference of 0.1% is added to the interband uncertainty. At 885 nm this discrepancy around the nominal 3% calibration is higher, of about 0.6%.

The total error budget is less than 0.6% from 681 to 865 nm and 1.3% at 885 nm due to extreme tests (coastal model at SPG), see Table 2. A maximum 1% uncertainty is assigned to all bands in DIMITRI interface. Because error on the input parameters can be considered as random (around true pressure, ozone, chlorophyll, etc.), this error budget contains mainly the random uncertainty, on punctual calibration points.

Table 2: Uncertainty budget of DIMITRI glint vicarious intercalibration coefficients in %, decomposed by sources. (*) comes from Hagolle *et al*. (1999)

Band	Ozone (*)	Pressure (*)	Aerosol model	AOT 865	Chl.	Pixel	Interband	Total
681	0.1	0.1	0	0.1	0.1	0.1	0.1	0.6
753		0.1	0.1	0.1	0.1	0.2	0.0	0.6
778		0.1	0.1	0	0.1	0.0	0.1	0.4
865		0.1	0	0.1	0.1	0.1	0.0	0.4
885		0.1	0.3	0.3	0.1	0.0	0.6	1.3

3.2.1 Tentative random/systematic uncertainty breakdown

Since vicarious calibration aims eventually at providing a unique set of coefficients, by averaging all targets, the uncertainty budget should rigorously be split into:

- The random uncertainty: its contribution to the averaged calibration coefficient goes down as more calibration points are considered
- The systematic uncertainty: its contribution remains the same whatever the number of points

No systematic source of error has been theoretically identified in previous uncertainty budget. Hence, we has tried to assess it experimentally, with real MERIS vicarious coefficients at SPG (most rigorous case study at present time due to knowledge of auxiliary data and proper radiative transfer LUT). Let us note σ the standard-deviation of a single target coefficient, i.e. the random uncertainty, and $\sigma(\overline{RA})$ the standard-deviation after averaging N targets; one has

$$\sigma(\overline{RA}) = \frac{\sigma}{\sqrt{N}}$$

(30)

Despite only few points are available (10), we observe that the experimental dispersion on $\overline{RA}$ does not follow this shape when N varies from 2 to 10. Assuming that the observed dispersion can be understood as the mean square error (MSE), we have searched the bias and random uncertainty following this decomposition:

$$MSE(N) = Bias^2 + \left(\frac{\sigma}{\sqrt{N}}\right)^2$$

(31)

In practice this is realised through a linear fit on $MSE(N) * N$. In order to avoid any statistical artefact when increasing the sample from N=2 to 10, we order it randomly and average over a large number of realisations (10 000).

Results of bias and σ are provided on Figure 4, and compared with previous sensitivity uncertainty budget. They remain very low, from 0.3% at 681 nm to 1.4% at 885 nm. Extrapolating these numbers on a large number of targets, i.e. decreasing at maximum the random contribution, results into a bias of less than 1%. This is very consistent with Hagolle *et al* (1999) estimates.

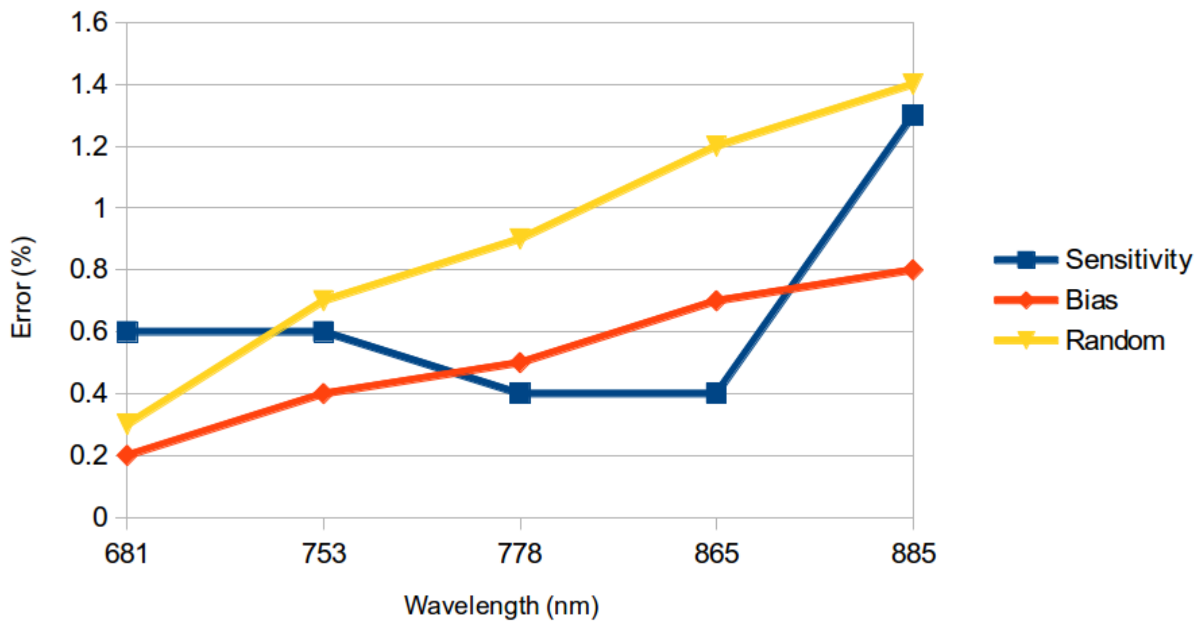

Figure 4 Tentative random (yellow)/bias(red) uncertainty breakdown of Sunglint vicarious method, based on MERIS vicarious coefficients at SPG. Blue uncertainty is from the sensitivity study of section 3.1.2

4 Implementation in DIMITRI_v3.0

4.1 Radiative transfer Look up tables (LUT)

4.1.1 Format specification in DIMITRI

For every sensor (i.e. every set of wavelengths and spectral response), DIMITRI Rayleigh calibration needs one Rayleigh LUT and four other LUT for each considered aerosol models: aerosol optical thickness dependence, downward total transmittance, upward total transmittance and path over Rayleigh fitting coefficients as function of optical thickness (previously noted XC in section 2.2.4).

All LUTs must be written in text file, with space as field separator, following the naming convention of

Table 3 to Table 7 below (AER may be any ASCII field identifying the aerosol model) and placed in directory AUX_DATA/RTM/SENSOR/. Any LUT satisfying this convention is detected by the GUI and can be used for the glint calibration. Reading and interpolation routines of DIMITRI_v3.0 are based on header description, giving size and discretisation of the LUT; this allows totally generic sampling in the LUT. Only the wavelengths must follow those of the considered sensor as defined in the Bin/DIMITRI_Band_Names.txt configuration file (NaN or any field may be used if some bands are not processed in the RTM).

Table 3: RHOR_SENSOR.txt template for Rayleigh reflectance LUT (PARASOL example)

```
# lambda: 443 490 565 670 763 765 865 910 1020
# thetas: 0.0 10.222899999999999 21.347999999999999 32.478999999999999
43.611400000000003 54.744399999999999 65.877600000000001 77.010999999999996 85.0
# thetav: 0.0 10.222899999999999 21.347999999999999 32.478999999999999
43.611400000000003 54.744399999999999 65.877600000000001 77.010999999999996 85.0
# deltaphi: 0.0 45.0 90.0 135.0 180.0
# wind: 1.5 5.0 10.0
# Inner loop is on wind, then deltaphi, thetav, thetas and bands
# Dimensions: 9 9 9 5 3
0.093101002156892598
…
```

Table 4: TAUA_SENSOR_AER.txt template for spectral dependence of aerosol optical thickness LUT at given AER model (PARASOL example for MAR-99)

```
# PARASOL aerosol optical thickness for aerosol MAR99
# Columns gives tau_a corresponding to 7 reference optical thickness at 550 nm, see DIMITRI ATBD Methodology for Vicarious Calibration
# (first optical thickness is zero)
# lambda: 443 490 565 670 763 765 865 910 1020
# Dimensions: 9 7
0.0 0.048365032840822532 0.06891816636709823 0.14085534900228486 0.34638948316831686 0.55199815122619944 0.8600978983396802…
```

Table 5: TRA_DOWN_SENSOR_AER.txt template for downward total transmittance LUT at given AER model (PARASOL example for MAR-99)

```
# PARASOL total downward transmittance (direct+diffuse, Rayleigh+aerosol) for aerosol model MAR99V
# Columns gives t_up for 7 aerosol optical thickness (total, i.e. all layers) given in file TAUA_PARASOL.txt
# (first optical thickness is zero hence gives Rayleigh transmittance)
# lambda: 443 490 565 670 763 765 865 910 1020
# thetas: 0.0 10.222899999999999 21.347999999999999 32.478999999999999
43.611400000000003 54.744399999999999 65.877600000000001 77.010999999999996 85.0
# Inner loop is on thetas, then on bands
# Dimensions: 9 9 7
0.90230878440213247 0.89548770811881195 0.89443874044173644 0.89082490644325962 0.88180250936785953 0.87149871603960372 0.85586978330540764…
```

Table 6: TRA_UP_SENSOR_AER.txt template for upward total transmittance LUT at given AER model (PARASOL example for MAR-99)

```
# PARASOL total upward transmittance (direct+diffuse, Rayleigh+aerosol) for aerosol model MAR99V
# Columns gives t_up for 7 aerosol optical thickness (total, i.e. all layers) given in file TAUA_PARASOL.txt
# (first optical thickness is zero hence gives Rayleigh transmittance)
# lambda: 443 490 565 670 763 765 865 910 1020
# thetav: 0.0 10.222899999999999 21.347999999999999 32.478999999999999
43.611400000000003 54.744399999999999 65.877600000000001 77.010999999999996 85.0
# Inner loop is on thetav, then on bands
```

```
# Dimensions: 9 9 7
0.90239652667174386 0.8954501151256663 0.89439713998476766 0.89094964438690016
0.88187861303884252 0.8717368052399086 0.85580240600152335…
```

Table 7: XC_SENSOR_AER.txt template for XC fitting coefficients LUT at given AER model (PARASOL example for MAR-99). Coefficients in column are respectively for the 0, 1 and 2-order term of the polynomial

```
# PARASOL XC coefficients of rhopath/rhoR fit against optical thickness for aerosol model MAR99V
# Columns gives the 3 XC coefficients
# Inner loop is on wind, then deltaphi, thetav, thetas and bands
# lambda: 443 490 565 670 763 765 865 910 1020
# thetas: 0.0 10.222899999999999 21.347999999999999 32.478999999999999
43.611400000000003 54.744399999999999 65.877600000000001 77.010999999999996 85.0
# thetav: 0.0 10.222899999999999 21.347999999999999 32.478999999999999
43.611400000000003 54.744399999999999 65.877600000000001 77.010999999999996 85.0
# deltaphi: 0.0 45.0 90.0 135.0 180.0
# wind: 1.5 5.0 10.0
# Dimensions: 9 9 9 5 3 3
1.0 2.002697662147753 -0.81783546808834739…
```

4.1.2 Atmospheric radiative transfer LUTs generation

This section describes the generation of the look-up tables of atmospheric path reflectance, total transmission and relative optical thickness over wavelength as required by both the Rayleigh calibration and the sunglint calibration in DIMITRI. The look-up tables required are almost identical in structure to those used in the MERIS atmospheric correction scheme (Antoine and Morel 2011, Barker *et al*. 2012), but must be generated for every band of every sensor contained in DIMITRI. Currently these bands cover wavelengths from 340 nm to 5000 nm. While the Rayleigh correction requires wavelengths up to 700 nm, plus some in the NIR for aerosol detection, the glint calibration requires these tables at all wavelengths. Since many of the sensors in DIMITRI cover the same wavelength ranges the approach that has been taken is to produce one overall hyperspectral look-up table that can be convolved to each sensor band using the relative spectral response function (RSR) of each band. This approach makes the modelling more efficient and has the benefit that if new sensors are added to DIMITRI their Rayleigh and glint calibration look-up tables can be generated without further modelling, as long as the wavelengths are in the range 340 to 5000 nm.

4.1.3 Computational considerations

As the values required are for a Rayleigh scattering based calibration it is required to calculate them to the highest accuracy possible, which means they must be fully vectorial (with polarisation) since scalar modelling can introduce deviations of a few percentage in Rayleigh scattering (Hedley *et al* . 2013). Here, we have used a modified version of the LibRadtran Monte Carlo model Mystic (Mayer and Kylling 2005; Mayer 2009). This model is capable of vectorial or scalar modelling and the vectorial mode Rayleigh scattering has been validated against both the MERIS atmospheric correction look-up tables and an independent model, Siro, developed at the Finnish Meterological Institute (Kujanpää 2013) (Figure 4).

The disadvantage of Mystic is that it is computationally slow, and being a Monte Carlo model is subject to statistical noise if insufficient computational effort is applied. In particular, with Mystic, each individual solar-view geometry requires a fully independent model run. Other models, such as the scalar Disort, can typically output results for a set of view zenith angles and relative azimuths for each run, but with Mystic one run must be done for every combination of solar, view and relative azimuth angles. These computational considerations are not trivial and require some compromises to be made. On a standard workstation, to produce results with the statistical convergence shown in Figure 4 takes approximately 15 seconds per Mystic run on average (the run time increases with aerosol optical thickness). The MERIS atmospheric correction look-up tables are tabulated over 25 zenith angles, 23 azimuth angles, 3 wind speeds, 7 aerosol optical thicknesses. If tables were to be generated at this resolution at 400 wavelengths, for example, then the computation time would be 25 x 25 x 23 x 3 x 7 x 400 x 15 seconds = 57 years. Therefore a compromise has been made in terms of the angular resolution of the modelling (Table 8). Modelling at every nanometre is unfeasible so 386 wavelengths from 340 – 5000 nm have been chosen as outlined in Table 8. This wavelength choice means that even the narrowest bands, MERIS at 9 nm, will have a minimum of two tabulated values within their RSR, but most will have many more. Conversely for bands that are wide this method ensures they are based on results spread across the band width. For the structure in Table 8, running the look-up table generation on a high-end workstation where calculation can be parallelised in up to 12 concurrent processes enables a look-up table for one aerosol model to be generated in approximately 4 weeks of compute time.

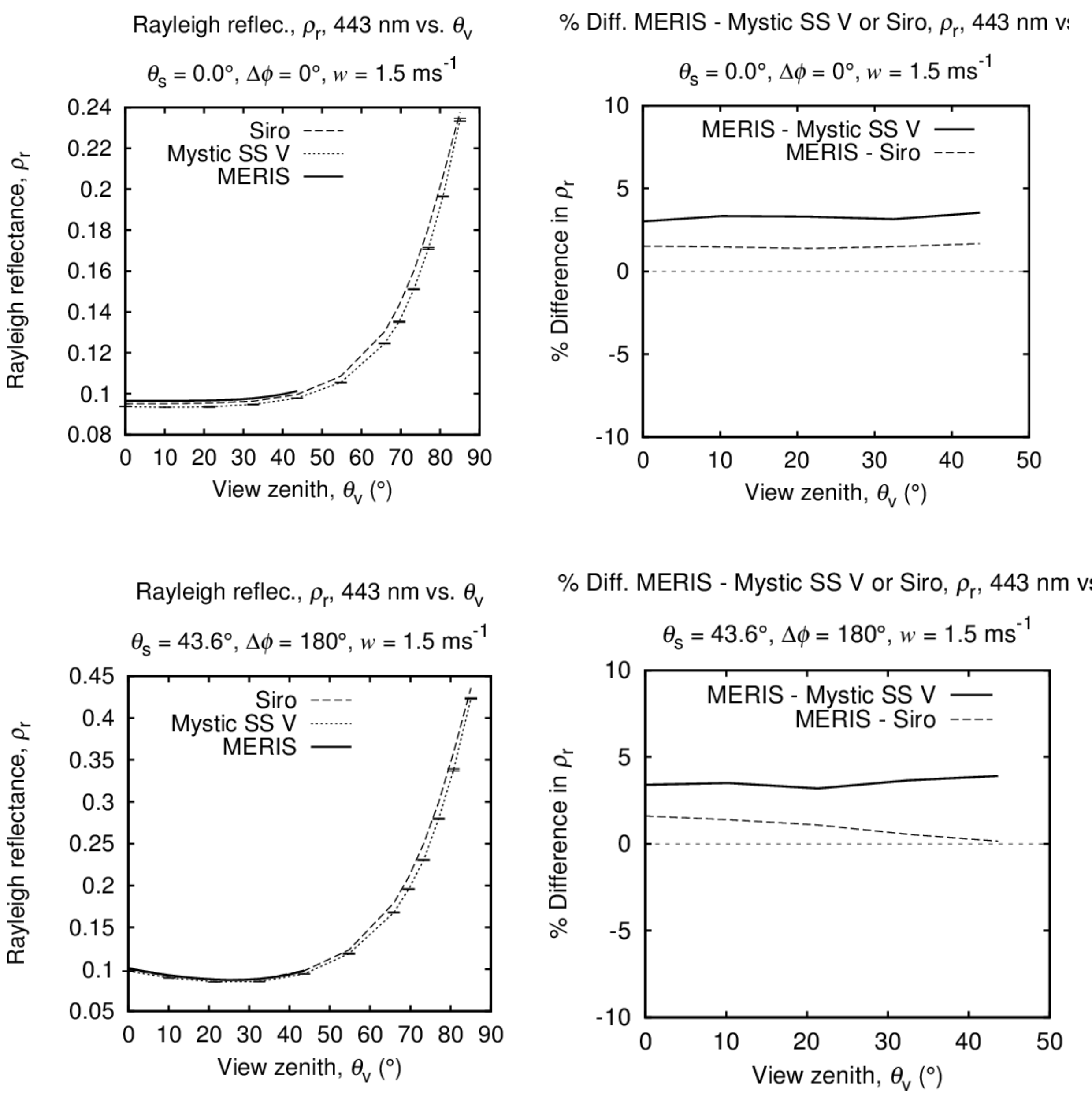

Figure 5: Example Rayleigh scattering results from Hedley *et al*. (2013) at 443 nm, from the MERIS atmospheric correction look-up tables and from Mystic and Siro in spherical shell vectorial mode.

Left side: Rayleigh scattering with error bars showing ±1 standard error on the mean for Mystic results. *Right side*: corresponding percentage difference between MERIS and Siro, and MERIS and Mystic.

Note: both Mystic and Siro predict an error of only one third of a percent due to plane parallel versus spherical shell modelling at zero solar and zenith angles, hence this is not an explanation for the small deviations of 2 – 3% seen here.

4.1.4 Details of the required tables

The required tables are as follows:

1. Atmospheric path reflectance

This is calculated over a 'black ocean', i.e. the bottom boundary is a wind-blown air water interface but below surface reflection is zero. The direct reflectance path from the surface is excluded so that the reflectance represents photons that have undergone one or more atmospheric scattering events. To evaluate this requires a modification to the Mystic code to exclude photons that have not undergone an atmospheric scattering event. Note gaseous absorption is also excluded in this calculation as this is corrected for elsewhere. What is actually stored in the look-up tables is the path reflectance, ρ_{path}, divided by the Rayleigh reflectance, ρ_r, as a function of aerosol optical thickness, fit to a quadratic function for each view and solar geometry, wind speed and sensor band. The quadratic fit is constrained so that the constant term is 1 as for $\tau_a(b) = 0$, $\rho_{path}(b) / \rho_r(b) = 1$ (where b is the sensor band). See Hedley *et al* (2013) for more information on the accuracy of this function fitting.

2. Total transmission, upward and downward

The product of the total transmission upward and downward is evaluated from Mystic using another modification that excludes photons that have not reflected from the bottom boundary. The model is run over a Lambertian bottom of diffuse reflectance 0.1, the total transmittance is then the reflectance divided by 0.1 and corresponds to the assumption that water-leaving reflectance has a Lambertian BRDF. This assumption, while not strictly accurate (Morel and Gentili, 1993), will have minimal impact in this context. The assumption of Lambertian sub-surface reflectance has been shown to introduce only small errors (Yang and Gordon, 1997), see further discussion on this issue in Hedley *et al.* (2013). In addition the Lambertian assumption allows decoupling of the upward and downward transmittances, since the bottom boundary reflectance only has a dependence on the cosine of the solar zenith angle. The algorithm input requires that the upward and downward total transmittances be tabulated separately, although it is only their product that is used (Eqn. 17). If the model is run with a full set of solar zenith angles with view angle fixed (e.g. at zero) and vice versa the individual upward and downward transmissions could be calculated except there is unavoidably an unknown scaling factor between the upward and downward transmissions. In other words, for n zenith angles, there are $2n$ unknowns, but only $2n$-1 values to derive these from. This can be solved by assuming the upward and downward transmissions at zenith angle zero are equal. Note this is simply a trick to enable the algorithm implementation to be supplied with separate tables for upward and downward transmittance. When the product is formed the unknown factor disappears and the correct total transmission is used in Eqn. 17 regardless of this assumption.

This reflectance-based method for deriving the transmittance is required and appropriate because: 1) Mystic in general lacks outputs from which the total transmittances can be easily computed, and 2) it is the inverse of the process that must be captured, i.e. the reconstruction of the TOA reflectance from the bottom boundary reflectance (Eqn. 17). Decoupling of the water leaving reflectance from the atmospheric radiative transfer is equivalent to assuming that higher order photon interactions at the bottom boundary are negligible, i.e. that a photon reflects once only from the water body and hence the TOA reflectance is a linear function of the water body reflectance. This is valid, at least for diffuse reflectances up to 0.1, as shown in Figure 5 (see also Hedley *et al* 2013).

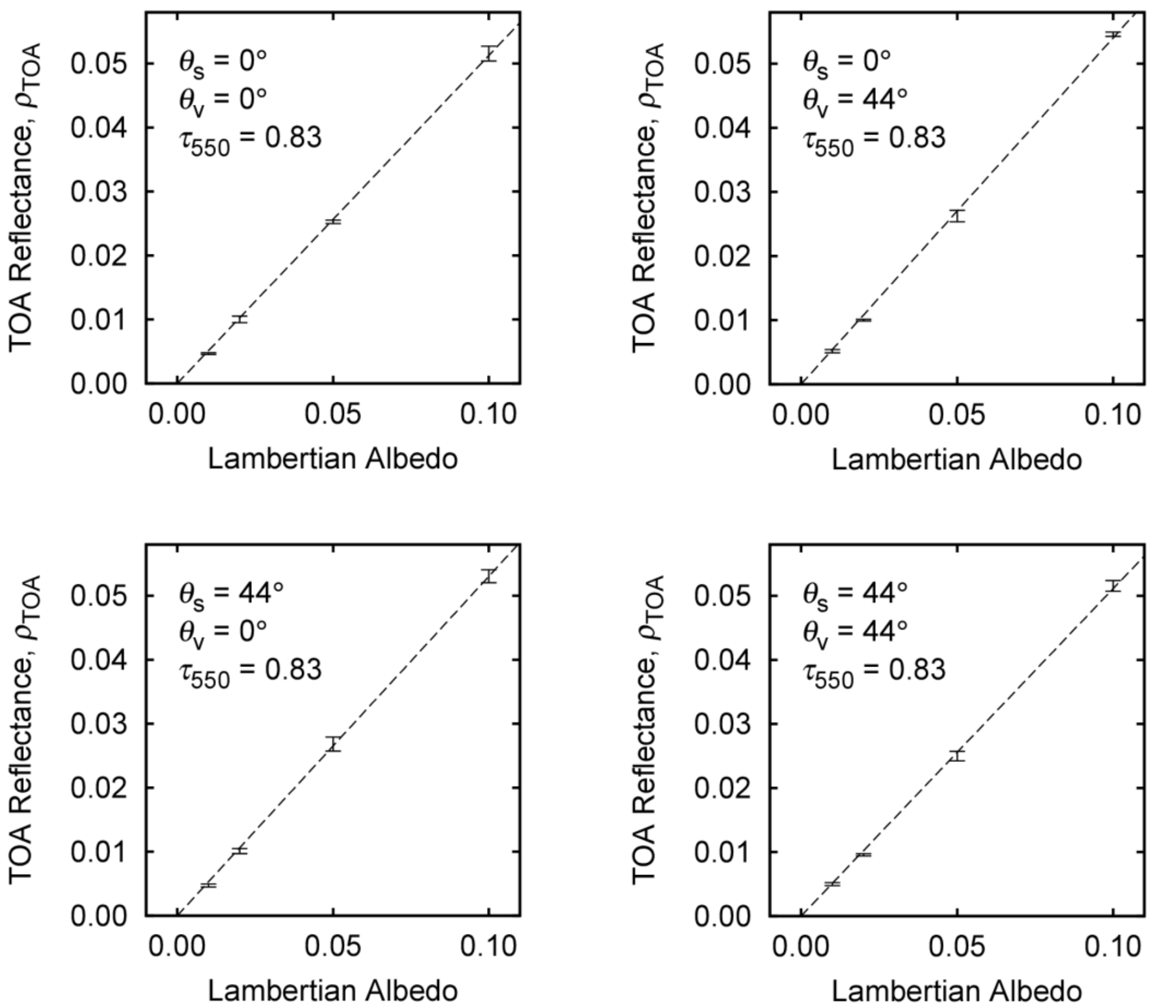

Figure 6: TOA reflectance from diffuse transmission paths as a function of bottom boundary Lambertian albedo from Hedley *et al*. (2013). These results were calculated in scalar spherical shell Mystic with the MAR-99 aerosol model (MERIS aerosol no. 4) τa (550) = 0.83, but the general conclusion of linearity with bottom reflectance will hold for plane parallel vectorial modelling. Error bars are ± 1 standard error on the mean, line is least squares linear fit.

3. Variation in optical thickness with band

The radiative transfer models are run with aerosol models of differing specified optical thicknesses at wavelength 550 nm. The algorithms require that the corresponding aerosol optical thickness can be derived for other bands. This table enables that transformation to be made, for a given sensor and aerosol model it relates the optical thickness in one band to the others. These values are not dependent on solar-view geometry or wind speed. The values at each wavelength are output directly in the libRadtran run log at each wavelength. The values for each sensor band are derived from the convolution by the sensor RSR.

4.1.5 Details of LibRadtran parameterisation

Certain details of the libRadtran parameterisation are listed below for reference. The next section describes the aerosol models.

- Standard US atmosphere 'AFGLUS'
- Atmospheric height 120 km
- Pressure 1013 mb
- No gaseous absorption
- Plane parallel configuration
- Vectorial scattering
- For black ocean, non-vectorial Cox-Munk wind-blown sea surface

Mystic can also be run in spherical shell mode, and even for solar and zenith angles of zero this can make a third of a percentage difference in the Rayleigh scattering, and for other solar-view geometries the deviation can rise to several percent (Hedley *et al*. 2013). While the LUT generation code permits switching to spherical shell mode, within the context of this project the 'traditional' plane parallel assumption has been made.

Similarly, while Mystic does incorporate a vectorial version of the sea surface BRDF function, the vast majority of previous work, such as the MERIS atmospheric correction LUTs, has utilised the non-vectorial mode Cox and Munk equations, and these are used here. Use of a vectorial sea surface function, or one that is more accurate in that it incorporates elevation statistics as well as slope (Kay *et al*. 2012) may be advisable, but is a potential future research topic.

Testing indicated that the Mystic options for forward or backward ray tracing and the 'vroom' optimisation did not reduce processing time or produce any overall improvement in statistical convergence. The 'escape' photon optimisation was enabled throughout.

Table 8: Structure of look-up tables for one aerosol model.

Parameter	Units	n	Values
λ	nm	386	340 to 1100 with step 4 (191), 1120 to 5000 step 20 (195)
θ_s	deg.	9	0, 10.2229, 21.3480, 32.4790, 43.6114, 54.7444, 65.8776, 77.0110, 85.0
θ_v	deg.	9	0, 10.2229, 21.3480, 32.4790, 43.6114, 54.7444, 65.8776, 77.0110, 85.0
$\Delta\phi$	deg.	5	0, 45, 90, 135, 180
wind	ms^{-1}	3	1.5, 5, 10
$\tau_a(550)$	-	7	0, 0.04, 0.06, 0.13, 0.33, 0.53, 0.83

Table 9: Components used in OPAC aerosol models as implemented in libRadtran (Hess *et al*. 1998)

Code	Meaning
inso	insoluble
waso	water_soluble
soot	soot
ssam	sea_salt_accumulation_mode
sscm	sea_salt_coarse_mode
minm	mineral_nucleation_mode
miam	mineral_accumulation_mode
micm	mineral_coarse_mode
mitr	mineral_transported
suso	sulfate_droplets

4.1.6 Aerosol models

Since generating a table for one aerosol model takes approximately 4 weeks of compute time, it is not trivial to add many aerosol models to the algorithm. Within the scope of the prototype algorithm three models have been incorporated.

- **MC50:** the OPAC Maritime clean model included in LibRadtran
- **MAR50:** the MERIS atmospheric correction aerosol model no. 1
- **MAR99:** the MERIS atmospheric correction aerosol model no. 4

Details of the aerosol model parameterisations are given in the following two sections. Figure 7 shows aerosol optical thicknesses as a function of wavelength for the three models, as output by LibRadtran, and indicates that MAR50 and MAR99 are correctly set-up as corresponding to the

MERIS atmospheric correction LUT models. Interestingly although the OPAC model MC50 is described as corresponding to 50% relative humidity in the LibRadtran documentation, it corresponds closely to MAR99, which is considered as 99% relative humidity. However the slope of MC50 starts to deviate in the Near-Infra Red, so it is worthwhile to retain it in the algorithm. MAR50 and MAR99 represent the extreme slopes in optical thickness from the MERIS maritime aerosol models, so candidate models for future inclusion might be MAR70 and MAR90 which represent intermediate slopes.

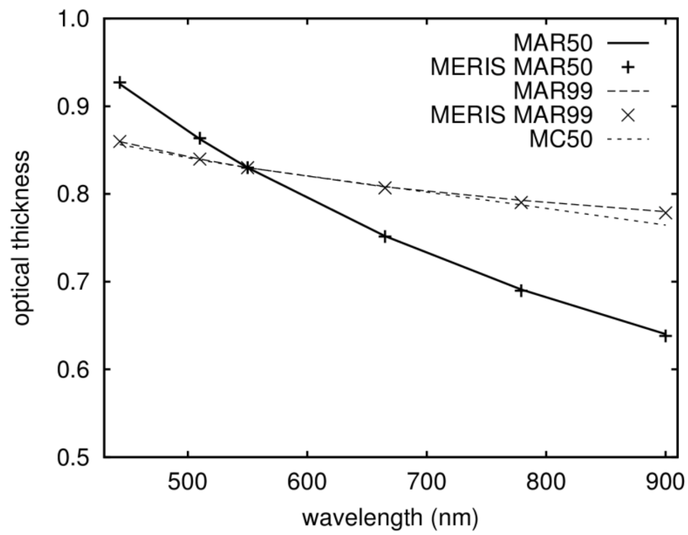

Figure 7: Aerosol optical thickness from 440 to 900 nm for the implemented aerosol models MAR50, MAR99 and MC50. Tabulated values for MAR50 and MAR99 from the MERIS atmospheric correction algorithm are also shown as point data.

MC50 - OPAC Maritime Clean Aerosol Model

The LibRadtran OPAC "Maritime clean" model (Hess *et al*. 1998) corresponds to relative humidity of 50% and as implemented in LibRadtran corresponds to a fixed vertical profile of six aerosol types specified up to 35 km, which combined have aerosol optical thickness of 0.136 at 550 nm. In order to generate a look up table parameterised over aerosol optical thickness, $\tau_a(550)$, it is necessary to scale the mass densities or some or all of the components. In the MERIS atmospheric correction aerosol models the way this is achieved is by holding constant the profiles above 2 km and scaling only the 0 – 2 km components, so this practice has been followed in the scaling of the OPAC MC50 model. MC50 in LibRadtran contains the following components (Table 9): inso, waso, soot, ssam, sscm, suso. Of these inso soot suso are only occur above 2 km, ssam and sscm occur only below 2 km and waso occurs up to 12 km but is 5-10 times denser below 2 km. Therefore splitting the model into variable 0 – 2 km profiles and fixed profiles above 2 km is supported by the construction of the model and involves only varying the water soluble and sea salt aerosols. In MC50 the fixed profiles above 2 km correspond to an aerosol optical thickness of 0.018, in comparison to 0.030 in the MERIS standard aerosol models 1-12. The default MC50 0 – 2 km profiles have an optical thickness of 0.119, and the mass densities in this fraction are scaled linearly to give the total $\tau_a(550)$ as required in the look up table construction (Table 8). The default MC50 corresponds approximately to the tabulated point $\tau_a(550) = 0.13$. The LibRadtran OPAC models are defined from 250 nm to 40 microns, hence in terms of wavelength coverage are more than adequate.

MAR50 and MAR99, the MERIS atmospheric correction models

These models have been constructed for use in vectorial mode Mystic by use of the Mie scattering tool supplied with LibRadtran. The size distributions and refractive indices of the model components used are specified in the MERIS RMD and original paper by Shettle and Fenn (1979). The Mie tool is used to generate the wavelength dependent Mueller matrices and single scattering albedos, and these are conveniently output in netCDF files that LibRadtran takes as input. An additional input file specifies the vertical profiles of the differing aerosol components, which for these models occur in three distinct layers, 0 -2 km, 2 -12 km and 12 – 50 km. Again, the relative proportions were fixed according to the values in the MERIS RMD (Barker *et al*. 2012), but the 0 - 2 km fraction was scaled to reach the required $\tau_a(550)$ values as in Table 8. The models were validated by checking the relative optical thicknesses at different wavelengths to those tabulated in the MERIS RMD. Barring numerical differences in the modelling and undocumented details in the parameterisation, the MAR50 and MAR99 models should correspond exactly to hyperspectral versions of models 1 and 4 in the MERIS atmospheric correction.

4.2 Auxiliary data for marine modelling

Pure seawater absorption and scattering coefficients come from the NASA ocean color repository: http://oceancolor.gsfc.nasa.gov/DOCS/RSR/water_coef.txt.

The table of averaged cosine for downwelling reflectance (μ_d in Morel (1988) and Morel and Maritorena (2001)) comes from Morel *et al*. (2006) available on LOV repository at oceane.obs-vlfr.fr/pub/morel. Other parameters of the Morel and Maritorena (2001) model are directly taken from their table 2.

Refractive index of pure seawater comes from MERIS tables (Barker *et al*. 2012) and is spectrally interpolated for any wavelength.

As suggested by the sensitivity analysis, deriving meaningful coefficients needs the most realistic chlorophyll estimate. Unfortunately we cannot fully benefit from the unique characterisation of oceanic calibration zones by Fougnie *et al*. (2002) because DIMITRI SPG and SIO sites do not exactly coincide with these regions. For SPG, we can still consider as last resort the characterisation of the South-East Pacific zone (PacSE); more precisely we use updated statistics of ACRI-ST reported on Figure 8, showing chlorophyll concentration variation between 0.045 and

0.075 mg/m3 along the year. In order to not slant the MERIS and MODIS calibration results, we only consider SeaWiFS time-series, monthly averaged in DIMITRI.

Such time-series cannot be created similarly for DIMITRI SIO site, located in a much more variable and richer region than IndS zone (Indian South) of Fougnie *et al*. (2002); in this case users can select a fixed value of their choice in DIMITRI HMI (see hereafter). Note that users can still add any chlorophyll climatology file, which would be automatically processed by DIMITRI.

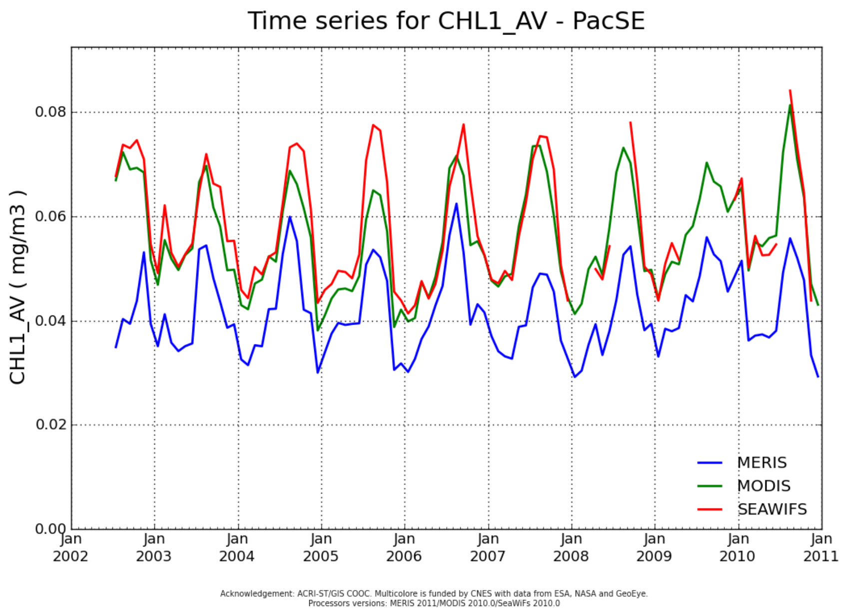

Figure 8 Time series of chlorophyll concentration over South-East Pacific calibration zones for MERIS, MODIS and SeaWiFS. Products and statistics processed by ACRI-ST and distributed on the GIS COOC data portal in the frame of the MULTICOLORE project, funded by CNES (MSAC/115277), using ESA ENVISAT MERIS data and NASA MODIS and SeaWiFS data.

4.3 Pixel-by-pixel versus averaged extraction

Whereas DIMITRI v2.0 database only stores spatially averaged L1b information per acquisition (array SENSOR_L1B_REF in SENSOR_TOA_REF.dat files for each site and sensor), DIMITRI v3.0 also retains the pixel-by-pixel extractions in new SENSOR_TOA_REF_PIX.dat files. In IDL, the parameters and dimensions of new arrays SENSOR_L1B_REF_PIX are based on former averaged SENSOR_L1B_REF arrays but:

- They include cloud mask as a new parameter. The list of parameters is thus: decimal_time, VZA, VAA, SZA, SAA, Cloud_mask, Ozone, Pressure, Humidity, Zonal_wind, Meridional_wind, Water_vapour, rho_band_0, …, rho_band_n
- They store each parameters for all individual pixels falling within the site, instead of the mean and standard-deviation; storage follows the same logics as averaged arrays when

more than one viewing directions is available (e.g. AATSR, ATSR2, PARASOL):

obs1_dir1_pix1, ..., obs1_dir1_pixO_1D_1, obs1_dir2_pix1, ..., obs1_dir2_pixO_1D_2, ...

where O_iD_j is the number of pixels for observation i in direction j.

It is worth noting that this number is in all generality variable through all observations and directions, because of variable sensor coverage of the site and variable pixel size in the swath. Also, there is no data screening of the pixels during the DIMITRI ingestion, contrary to the average restricted to valid pixels (validity based on radiance thresholds only, not cloudiness).

As a consequence the size of new SENSOR_TOA_REF_PIX.dat files (one per site and sensor/processing version) is substantially bigger than that of SENSOR_TOA_REF.dat but still largely lower than the archive of raw L1b product. As an example, the total size of current MODIS archive over SPG site is:

- 2.7MB in averaged extraction file,
- 1.5GB in pixel-by-pixel extraction file, and
- 167 GB in raw L1B files.

The pixel-by-pixel extractions allow vicarious calibration coefficients to be computed on exact pixel radiometry, then averaged per scene. This is important for the glint calibration because of small scale of sea surface roughness; Figure 9 is an example of MERIS scene allowing wind speed inversion in pixel-by-pixel mode and not when averaged.

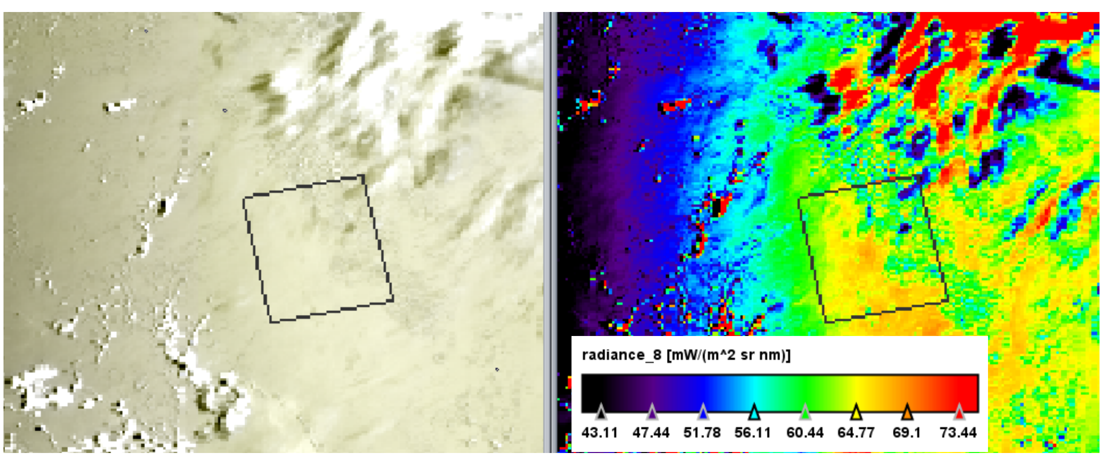

Figure 9: Sun glint pattern observed by MERIS over SPG (within black square) on 15 January 2011. Left is Level 1 RGB and right Level 1 radiance at 680 nm showing pixel-by-pixel variability.

The user is given the choice to select either this pixel-by-pixel extraction or the standard DIMITRI averaged extraction (see HMI updates hereafter).

4.4 Output files generated by the glint intercalibration

Six types of files are systematically generated for each glint vicarious calibration run:

1. **GLINT_CAL_LOG.txt:** log file summarising all options of the run (parameters).
2. **GLINT_CAL_SITE_SENSOR_PROC_AVG.dat:** IDL SAV file storing array VIC_COEF_AVG of averaged vicarious coefficients per observation (when pixel by pixel mode) or directly coefficients starting from the averaged TOA signal (if not) and associated uncertainties. Consistently with the standard SENSOR_TOA_REF.dat DIMITRI files, parameters of VIC_COEF_AVG array are:

   decimal_time, VZA, VAA, SZA, SAA, Ozone (avg+stddev), Pressure (avg+stddev), Humidity (avg+stddev), Zonal_wind (avg+stddev), Meridional_wind (avg+stddev), Water_vapour (avg+stddev), DAk_band_0, …, DAk_band_n, DAk_unc_band_0,…DAk_unc_band_n

3. **GLINT_CAL_SITE_SENSOR_PROC_AVG.csv:** same as previous but in csv format for direct reading.
4. **GLINT_CAL_SITE_SENSOR_PROC_STAT.csv:** csv file containing statistics on the final unique set of coefficients per wavelength (median, mean, standard-deviation, number of points, mean uncertainty).
5. **GLINT_CAL_SITE_SENSOR_PROC_MEAN.JPG**: plot of the mean coefficients as a function of wavelength.
6. **GLINT_CAL_SITE_SENSOR_PROC_WAV.JPG:** plots for each wavelength: of the time-series of averaged coefficients.

When the pixel-per-pixel mode is activated, another output is:

7. **GLINT_CAL_SITE_SENSOR_PROC_PIX.dat:** IDL SAV file identical to the _AVG.dat one's but providing information for all individual pixels, consistently with input SENSOR_TOA_REF_PIX.dat file. It stores array VIC_COEF, whose parameters are:

   decimal_time, VZA, VAA, SZA, SAA, Cloud_mask, Ozone, Pressure, Humidity, Zonal_wind, Meridional_wind, Water_vapour, DAk_band_0, …, DAk_band_n, DAk_unc_band_0,…DAk_unc_band_n

   Averaged calibration coefficients per observation are exactly identical to the coefficients of VIC_COEF_AVG array provided in _AVG.dat file.

4.5 DIMITRI modules/functions/architecture

The glint calibration methodology is implemented as an individual IDL module, called by a new GUI module (or directly in command line); it then calls several separated routines for specific jobs (e.g. computation of Rayleigh reflectance, of marine models, etc.). All routines related to the glint vicarious calibration are stored in the Source/vicarious directory. Except for the GUI, there is no interaction with previous DIMITRI_v2.0 modules.

Schematically, the main glint calibration module:

- Interfaces with the DIMITRI database to identify appropriate L1b extractions with respect to chosen region, sensor, processing version and year;
- Screens data for ROI cloud and region coverage; in the pixel-by-pixel mode, pixels are further screened by the cloud mask;
- Finds all pixels within other user defined parameters specific to the calibration method;
- Reads all RTM LUT;
- Performs the glint calibration band per band;
- Post-processed the coefficients (averaged, statistics);
- Outputs the individual and averaged calibration coefficients for each band in several text and image file, as defined in section 4.4.

4.6 HMI updates and User options

The glint calibration methodology allows both GUI and command line activation. The main DIMITRI window is updated for using GUI mode (Figure 10).

All processing parameters specific to the glint calibration are selectable by the user through a new window (Figure 11):

- Case study (region, sensor, processing version, year, output directory);
- Cloud and region coverage percentage; note that scenes having a manual cloud screening set to 0 will be selected whatever the automated cloud screening value;
- Pixel-by-pixel mode;
- Chlorophyll concentration, either by monthly climatology put in the DIMITRI auxiliary folder or by a fixed values;
- Maximum wind speed;
- Maximum angle between viewing and specular directions;
- Reference band for the calibration;
- Absolute calibration coefficient for the reference band; this coefficient must be understood as in the Rayleigh absolute calibration (RAk, see Barker *et al* 2013b), i.e.

$$\rho_{TOA}^{cal}(\lambda_{ref}) = \rho_{TOA}^{obs}(\lambda_{ref})/RAk(\lambda_{ref}) \quad (30)$$

- Aerosol optical thickness at 865 nm;
- Aerosol model, among an automated list built on all models existing in DIMITRI auxiliary folder, sensor per sensor.

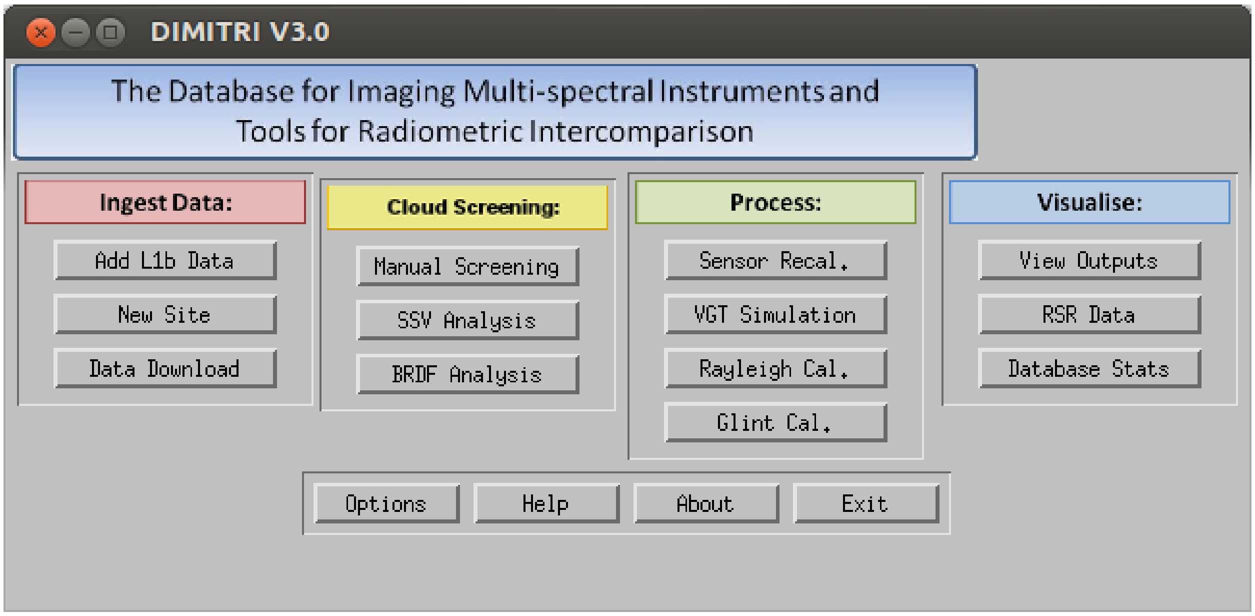

Figure 10: Main DIMITRI window updated for Rayleigh scattering and Sunglint vicarious calibration methods

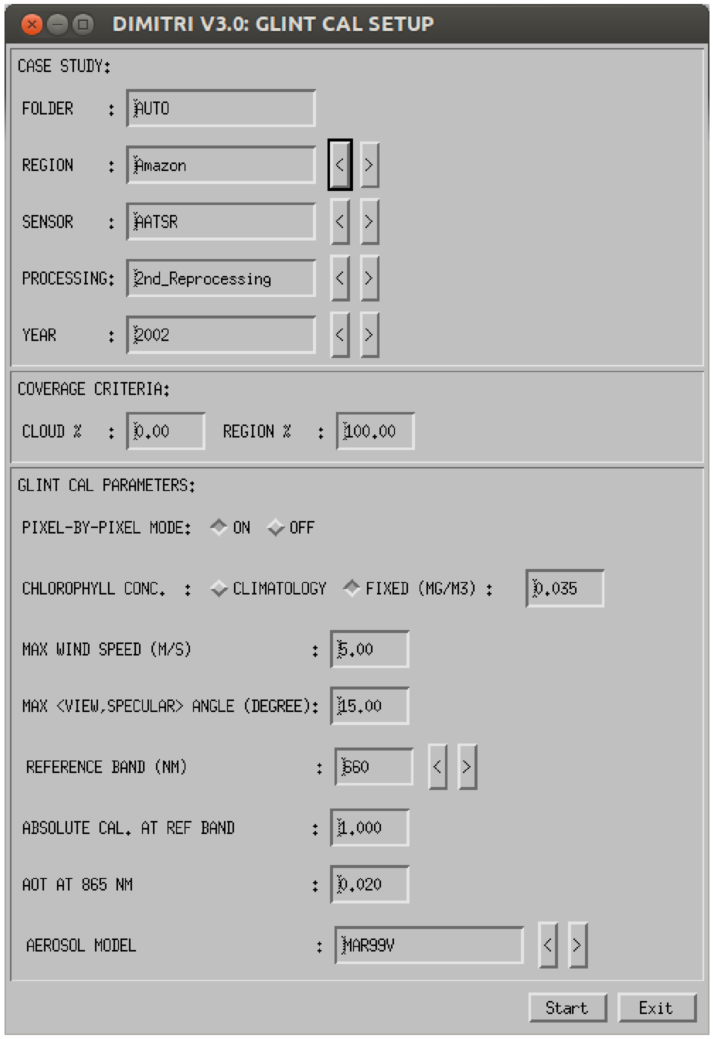

Figure 11: New DIMITRI window for parameterising the glint vicarious calibration

5 Results and implementation comparisons

Note: Wind speed modulus and gas concentrations used for atmospheric quantities computation come from DIMITRI auxiliary data associated to each measurement, as stored in SENSOR_TOA_REF.dat files. Because current DIMITRI version only provides these auxiliary data for MERIS, default values of w_m=5m/s and O_3=300 DU are automatically selected in order to present results for all sensors.

In all following results default options of the glint calibration are used, unless specified:

- Pixel-by-pixel mode
- 0% ROI cloud coverage,
- 100% ROI coverage,
- Maximum wind modulus of 5 m/s,
- Maximum angle between viewing and specular direction of 15°,
- Reference band chosen at 665 nm,
- Aerosol optical thickness at 865 nm of 0.02 and MAR-99 aerosol model.

Over SPG, chlorophyll concentration comes from previously detailed climatology. Over SIO, which does not provide such data, we follow the initial Hagolle *et al*. (1999) strategy by computing two sets of gains for extreme concentrations (0.035 and 0.17 mg/m3) and then average the gains.

5.1 DIMITRI implementation results for MERIS

The mean coefficients over SPG for MERIS 3rd reprocessing are detailed in Table 10 and plotted against wavelength on Figure12, taking an absolute calibration coefficient at 665 nm of 1.026, as found with Rayleigh scattering calibration (see Barker *et al* 2013). Coefficients present a slight linear spectral variation, except at 885 nm, and values from –2.9% at 681 nm to -1.6% at 865 nm and -0.6% at 885 nm. Being outside the estimated 2% error budget of the on-board L1b calibration (Bourg and Delwart, 2012) for red bands is directly due to the choice of calibration coefficient at reference band 665 nm, hence to the Rayleigh scattering result. It should be highlighted that only 11 observations on the full DIMITRI archive satisfies the screening criteria. The standard-deviation is relatively weak (0.5% max at 885 nm), compared for instance to the DIMITRI Rayleigh calibration and largely within the mean uncertainty (1%). This can be also seen on the time-series plots (Figure 13), showing a perfect alignment of all coefficients from 2002 to 2012.

Table 10: MERIS 3rd reprocessing glint intercalibration coefficients over SPG, relative to 665 nm

Band (nm)	Median Ak	Mean Ak	Standard-deviation	Mean uncertainty	N
665.00	0.975	0.975	0	0.01	11
681.00	0.971	0.971	0.002	0.01	11
753.00	0.977	0.977	0.003	0.01	11
778.00	0.98	0.981	0.004	0.01	11
865.00	0.984	0.984	0.005	0.01	11
885.00	0.993	0.994	0.005	0.01	11

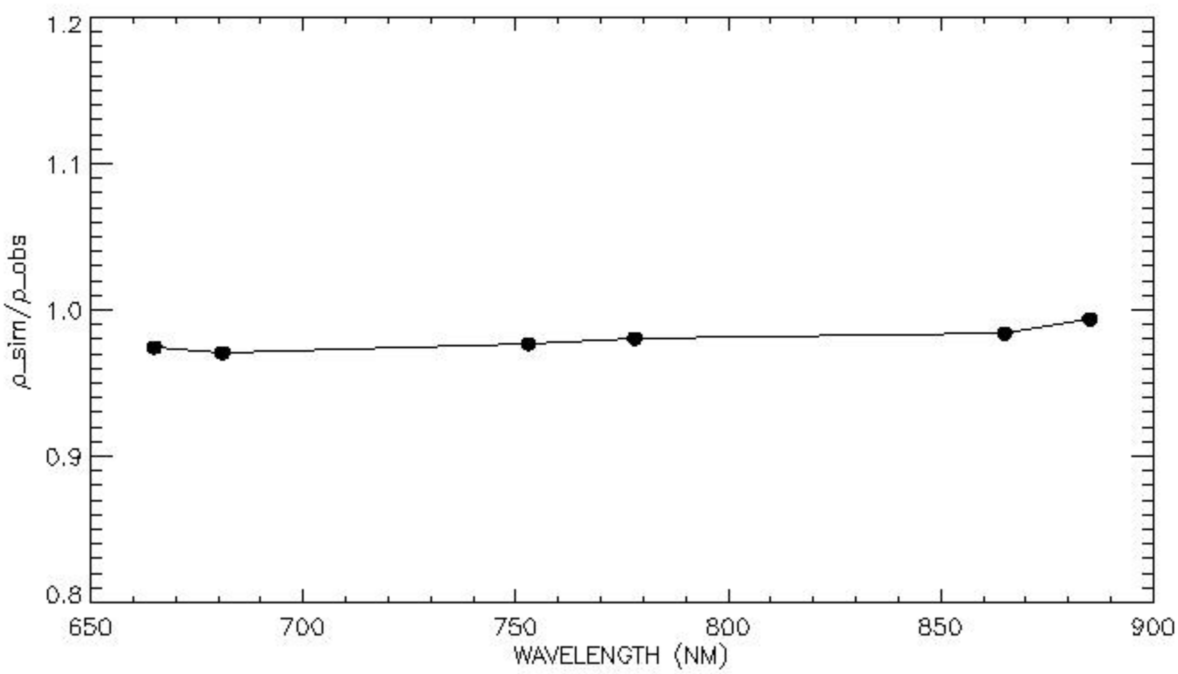

Figure 12: Mean MERIS 3rd reprocessing glint intercalibration coefficients (665 nm as reference) over SPG as a function of wavelength

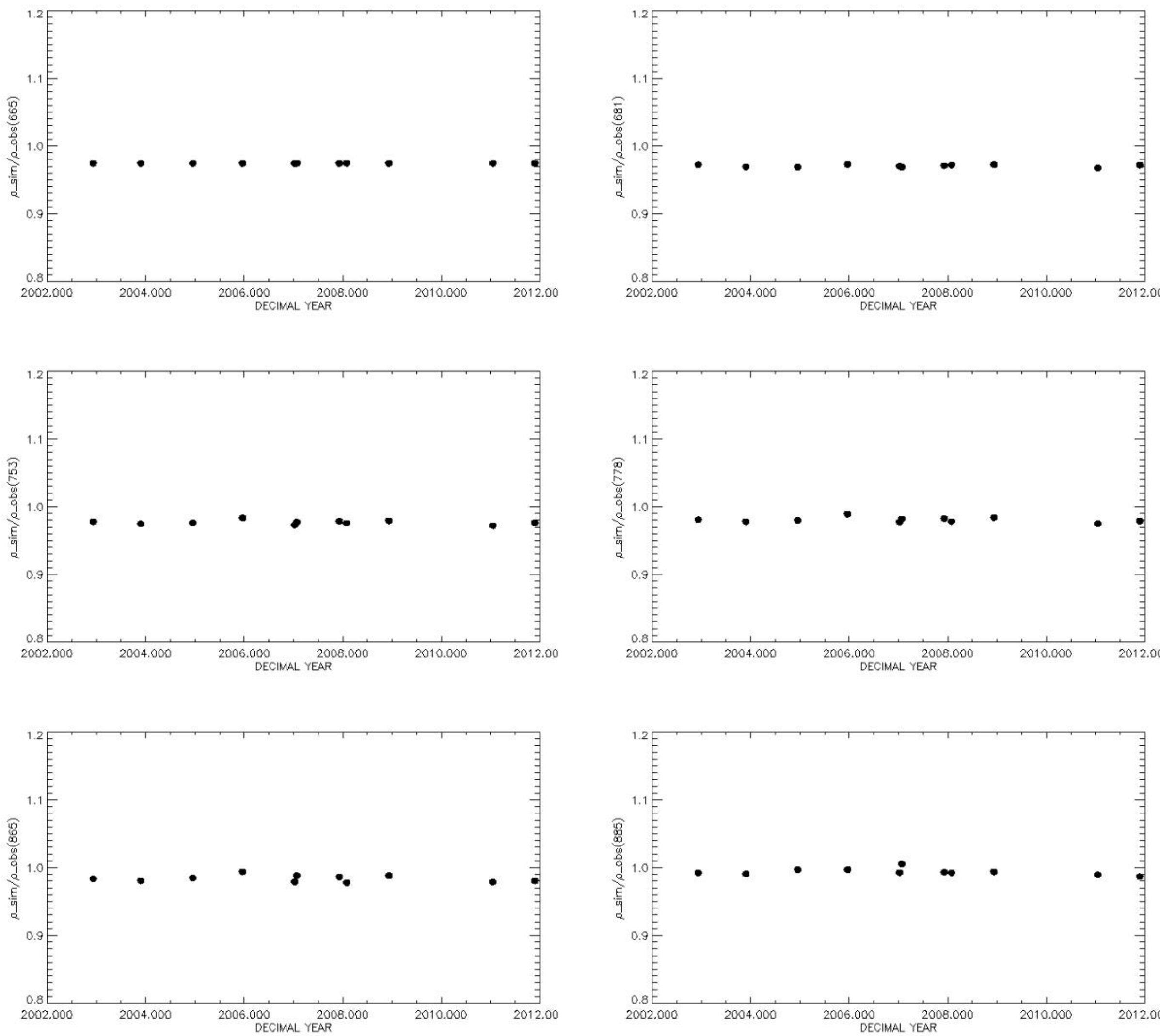

Figure 13: Times series of MERIS 3rd reprocessing glint vicarious intercalibration coefficients (665 nm as reference) over SPG at respectively 665, 681, 753, 778, 865 and 885 nm from top to bottom, left to right.

The coefficients are very comparable at SIO with a chlorophyll concentration of 0.035 mg/m3 (we remind here that there is very little effect of this parameter), see Table 10 and Figure 14, although only three observations were found.

Table 11: MERIS 3rd reprocessing glint intercalibration coefficients over SIO, relative to 665 nm

Band (nm)	Median Ak	Mean Ak	Standard-deviation	Mean uncertainty	N
665.00	0.975	0.975	0	0.01	3
681.00	0.97	0.97	0.001	0.01	3
753.00	0.974	0.974	0.001	0.01	3
778.00	0.977	0.977	0.002	0.01	3
865.00	0.978	0.978	0.002	0.01	3
885.00	0.985	0.986	0.004	0.01	3

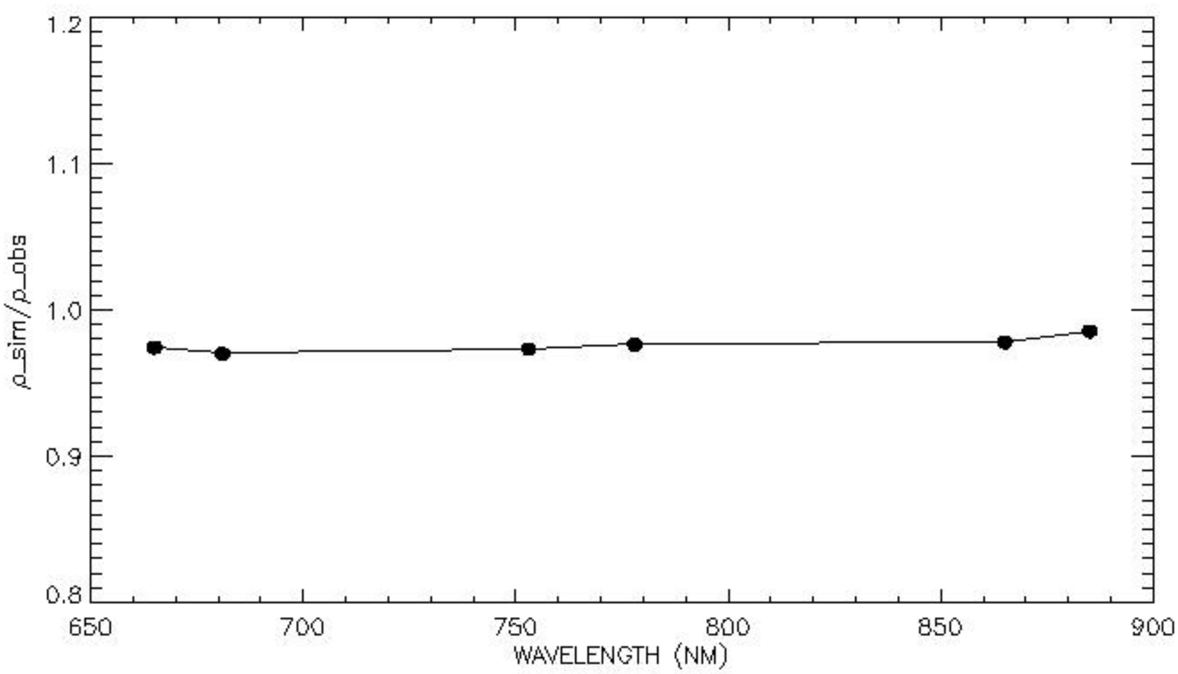

Figure 14: Mean MERIS 3rd reprocessing glint intercalibration coefficients (665 nm as reference) over SIO as a function of wavelength

Comparison with nominal vicarious coefficients of MERIS 3rd reprocessing (Lerebourg *et al*, 2011) is shown on Figure 15, where the DIMITRI Rayleigh vicarious calibration at 665 nm is expressed in term of Ak=1/RAk. Both methods disagree in term of shape towards near-infrared; however tests with MERIS RTM LUTs (not shown here) would again produce different results and conclusion. Furthermore we remind here that both approaches differ by a major interband assumption: Lerebourg *et al*. (2011) assumes that bands 779 nm and 708 nm (this latter not considered in DIMITRI) are perfectly calibrated (coefficients set to 1), for calibrating other near-infra red bands, in particular 865 nm.

In all cases the standard deviation are excellent, as already stated (if not visible on the plot), contrary to those of the Rayleigh calibration, and even better than the nominal MERIS vicarious in the near-infrared.

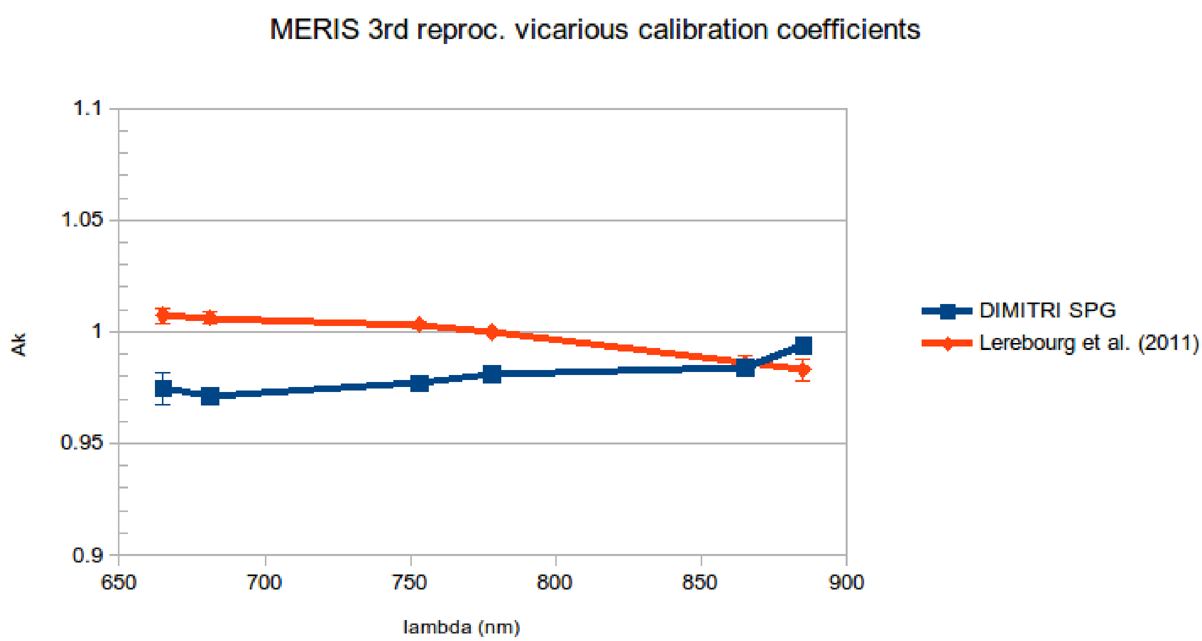

Figure 15: MERIS 3rd reprocessing mean gains as of DIMITRI Rayleigh calibration(blue line from 412 to 665nm, expressed in term of 1/RAk) and DIMITRI glint intercalibration relative to 665 nm (blue line from 681 to 885 nm) over SPG and for nominal MERIS vicarious calibration (red line, from Lerebourg *et al*., 2011).

In order to compare DIMITRI results with CNES computation of Fougnie *et al*. (2012), we compute the glint intercalibration coefficients of MERIS 2nd reprocessing starting from 620 nm, adjusted by a factor RAk=1.022 found by Rayleigh calibration (Figure 15). Values are actually comparable to those presented for 3rd reprocessing (yet relative to the 665 nm), around -2%. They are in relatively good agreement with CNES coefficients (Figure 17, expressed in term of RAk=1/Ak), yet these latter never exceed 2%. It is important to keep in mind that Fougnie *et al*. (2012) consider at least six oceanic regions.

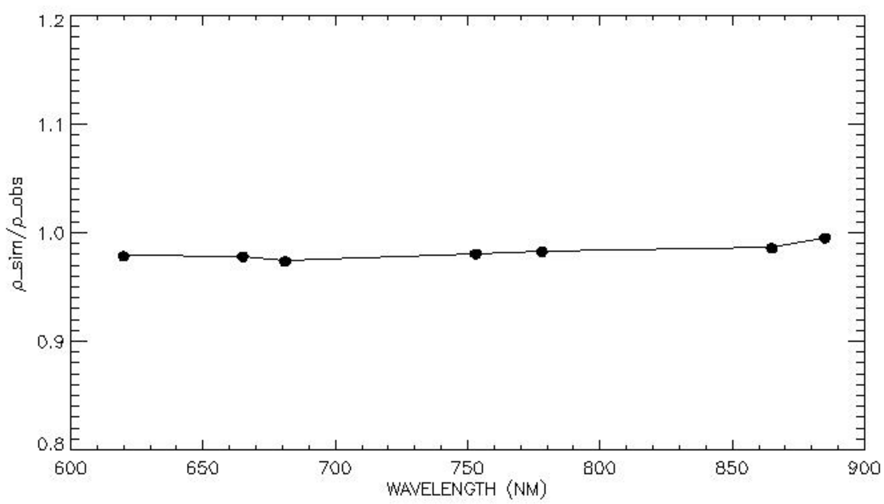

Figure 16 DIMITRI glint vicarious coefficients at SPG for MERIS 2nd reprocessing relative to 620 nm

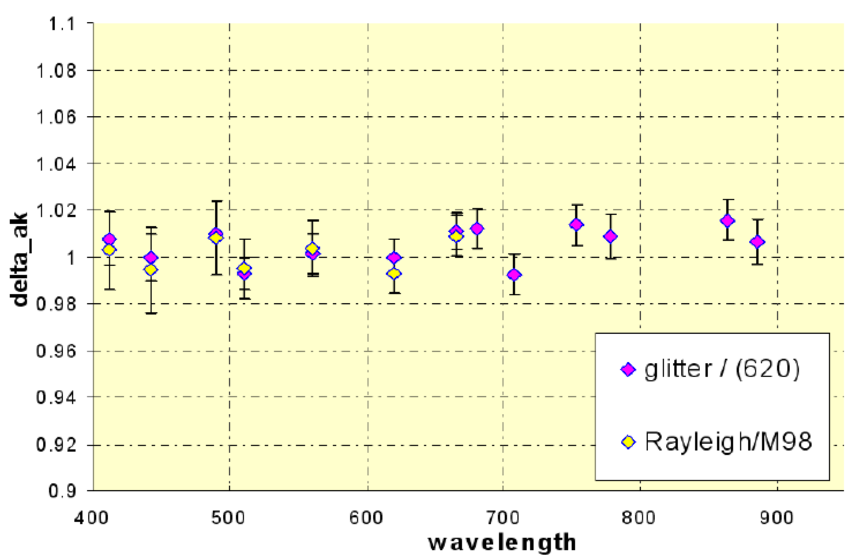

Figure 17: CNES glint vicarious intercalibration coefficients (pink symbols) for MERIS 2nd reprocessing relative to 620 nm. From Fougnie *et al* 2012

5.2 Preliminary DIMITRI implementation results for other sensors

Glint intercalibration coefficients over SPG for MODIS and PARASOL are displayed on Figure 18 and Figure 19 respectively. We recall here that the meteorological auxiliary data do not currently exist for these sensors, hence following results should be considered as preliminary. No AATSR, ATSR2 and VEGETATION products were found in current DIMITRI database satisfying the data screening for glint calibration.

We use the Rayleigh vicarious coefficient at the reference band, RAk(666)=1.024 for MODIS and RAk(670)=1.047 for PARASOL (median value). For this sensor, the near-infrared relative gain at 865 nm is consistent with Fougnie *et al* (2012) despite difference in Rayleigh absolute coefficients; its dispersion is also much lower, possibly because only one direction is selected over glint geometry, whereas Rayleigh calibration averages coefficients over several directions.

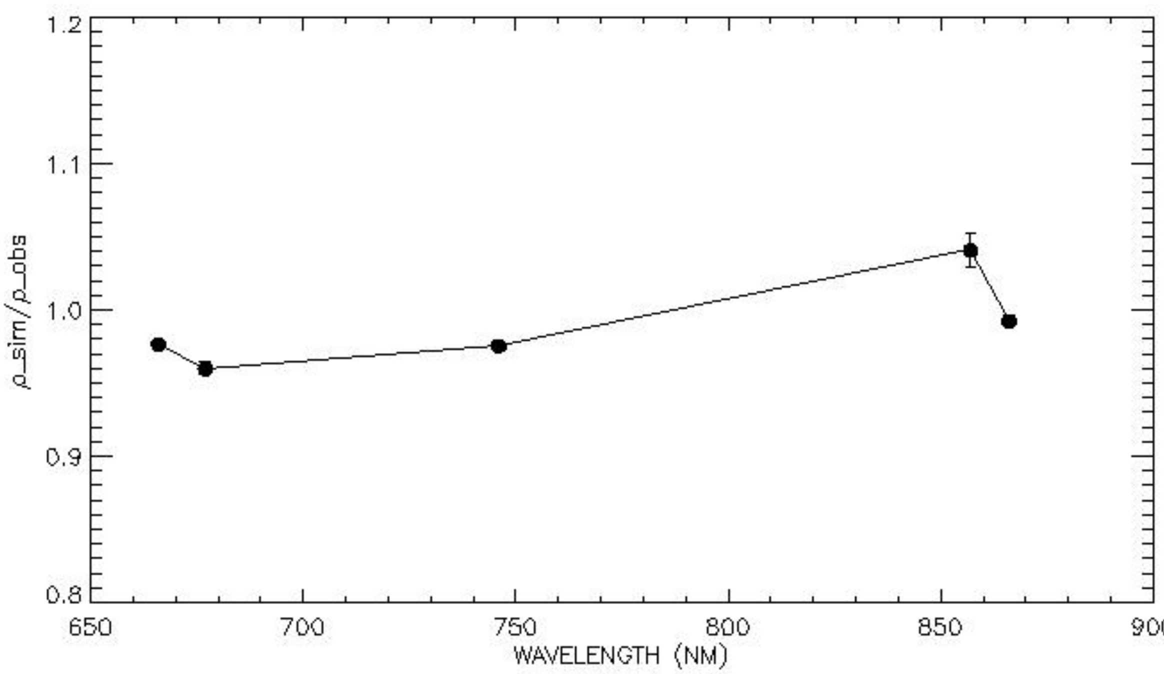

Figure 18: MODIS calibration coefficients over SPG.

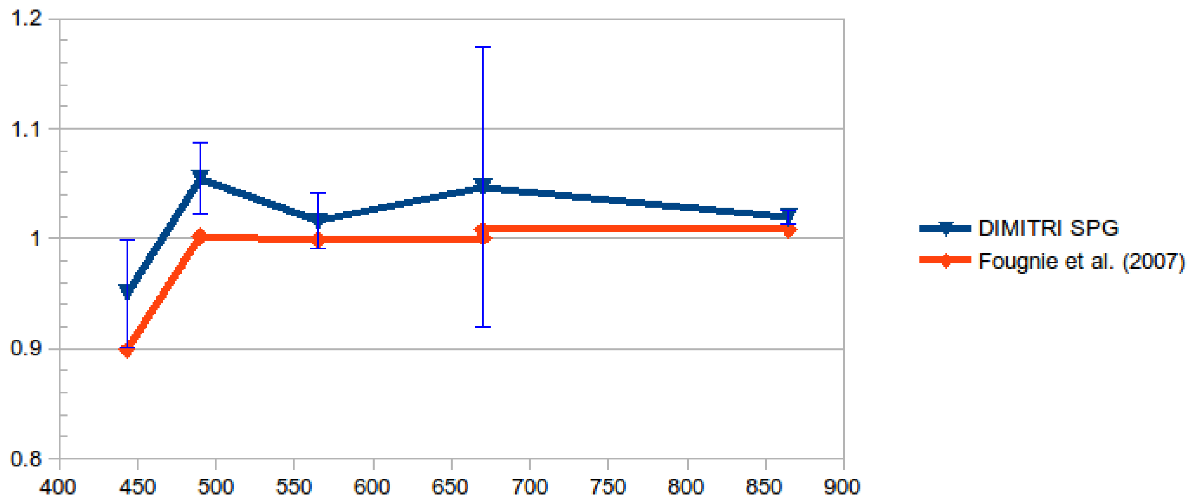

Figure 19: PARASOL vicarious calibration coefficients over SPG for DIMITRI (blue) and from Fougnie *et al* (2007) (red). Rayleigh method from 443 to 670 and glint method at 670 and 865 nm.

6 Discussion and conclusion

The glint calibration method implemented in DIMITRI_v3.0 follows essentially the initial work of Hagolle *et al*. (1999), with several adaptations taking into account more recent and well-tried ocean colour modelling in marine reflectance and aerosol contribution. A noticeable difference is that the aerosol optical thickness cannot be computed from simultaneous off-glint observations and is therefore fixed for once and all. It is a similar solution as in Hagolle *et al*. (2004) for VEGETATION, however the present methodology further screen the pixels after glint estimates to only keep those with consistent aerosol modelling in the near-infrared.

The DIMITRI_v3.0 HMI allows users to easily choose all main parameters of the calibration (thresholds, chlorophyll concentration, aerosol model, etc.). Automated handling of auxiliary files also gives users the possibility to immediately test other parameterisations of the signal modelling, both for the marine contribution, e.g. chlorophyll climatology, coefficients of the Morel and Maritorena (2011) model and atmospheric component (e.g. new look-up tables with different geometrical discretisation or aerosol models).

Vicarious coefficients presented here for MERIS are a slightly higher than the 2% expected L1b calibration uncertainty (Bourg and Delwart, 2012), but this is relative to the 2.6% calibration factor of reference band coming from Rayleigh scattering methodology. Taking a 0% factor at 665 nm produces a set of coefficients very close to unity from 681 to 885nm. This shows the importance of ensuring a perfect calibration at reference band. Also taking into account water vapour absorption would probably improve the results in the NIR bands.

It appears that the glint coefficients in the red and near-infrared are extremely stable along the years (very low standard-deviation), contrary to the Rayleigh vicarious calibration in the visible. This probably comes from the very strong and well-modelled glint signal at the reference band, contrary to the off-glint marine signal in the visible bands highly sensitive to the chlorophyll content.

Results and analysis have shown the necessity to increase the number of calibration points (in particular no data are found for AATSR, ATSR2 and VEGETATION-2). We recommend enriching the DIMITRI database with oceanic targets studied in Fougnie *et al*. (2002) and used in Fougnie *et al*. (2012).

In order to get finalised coefficients of all sensors, we recommend running the glint calibration with meteorological auxiliary data for AATSR, ATSR2, MODIS, PARASOL and VEGETATION-2.

7 References

Antoine, D. and A. Morel (1999). A multiple scattering algorithm for atmospheric correction of remotely-sensed ocean colour (MERIS instrument): principle and implementation for atmospheres carrying various aerosols including absorbing ones, IJRS, 20, 1875-1916.

Antoine, D. and Morel, A. (2011). MERIS ATBD 2.7 Atmospheric Correction of the MERIS observations Over Ocean Case 1 waters. Technical Report MERIS ATBD 2.7 v5.1-July2011 (Version 5.1).

Barker, K., Marrable, D., Hedley, J., Mazeran, C. (2013) Rayleigh scattering methodology for vicarious calibration, DIMITRI ATBD ref. MO-SCI-ARG-TN-004b, Issue 1.0

Barker, K., Antoine, D., Bourg, L., Brockmann, C., Doerffer, R., Fischer, J., Moore, G., Santer, R., and Zagolski, F. (2012). Reference Model for MERIS Level 2 Processing. Third MERIS reprocessing: Ocean Branch. Technical Report PO-TN-MEL-GS-0026 (Version 5.2)

Bourg, L. and S. Delwart (2012) MERIS instrument calibration. Available at http://earth.eo.esa.int/pcs/envisat/meris/documentation/

Bouvet, M. (2006). Intercomparisons of imaging spectrometers over the Salar de Uyuni (Bolivia). *Proc. 2nd MERIS and AATSR Calibration and Geophysical Validation Meeting (MAVT-2006)*, 20-24 March 2006, ESRIN.

Bouvet, M. (2011). Simulation of VEGETATION measurements with DIMITRI. ESA Tech. Note: TEC-EEP/2011.713/MB

Bouvet M., Goryl P., Chander G. Santer R., and Saunier S. 2007. Preliminary radiometric calibration assessment of ALOS AVNIR-2. Proc. Geoscience and Remote Sensing Symposium, IGARSS 2007

Cox, C., and W. Munk (1954), Statistics Of The Sea Surface Derived From Sun Glitter, J. Mar. Res., 13, 198 – 227

Fougnie, B., Patrice Henry, P., Morel, A., Antoine, D., Montagner, F. (2002). Identification and characterization of stable homogenous oceanic zones: climatology and impact on in-flight calibration of space sensors over rayleigh scattering. Ocean Optics XVI, Santa Fe, NM.

Fougnie, B., Bracco, G., Lafrance, B., Ruffel, C., Hagolle, O., Tinel, C. (2007) PARASOL in-flight calibration and performance, Applied Optics, Vol. 46, No 22, 5435-5451

Fougnie, B., Henry, P., Lachérade, S., and P. Gamet (2012) Radiometric calibration of desert sites and oceanic target. Sentienl-3 calibration and validation planning meeting, ESA/ESRIN, March 2012.

Hagolle *et al*. (1999) Results of POLDER in-flight Calibration, IEEE Transactions on Geoscience and Remote Sensing, May 1999, Volume 37, Number 03

Hagolle, O., JM. Nicolas, B. Fougnie, F. Cabot, P. Henry. 2004. “Absolute Calibration of VEGETATION Derived From an Interband Method Based on the Sun Glint Over Ocean”, IEEE Transactions On Geoscience And Remote Sensing, Vol. 42, No. 7

Hansen, J.E. and L. Travis, 1974. Light scattering in planetary atmospheres, Space Science Reviews, 16: 527-610.

Hedley J, Lamquin N, Mazeran C. (2013) Atmoshperic Correction for Ocean Colour in a Spherical Shell Atmosphere. Algorithm Theoretical Basis Document. ESA Report GEOHR-D6 AO/1-7084/12/NL/AF (Version 0.9.2).

Hess M, Koepke P, Schult I (1998) Optical Properties of Aerosols and Clouds: The software package OPAC. Bulletin of the American Meteorological Society 79(5) 831-844.

Kay, S., Hedley, J., Lavender, S., and Nimmo-Smith, A. (2011). Light transfer at the ocean surfacemodelled using high resolution sea surface realizations. Opt. Express, 19(7):6493–6504.

Kou, L., D. Labrie, P. Chylek, 1993, "Refractive indices of water and ice in the 0.65-2.5 m spectral range," Appl. Opt.,32, 3531-3540 (1993).

Kujanpää, J. (2013). Atmospheric Correction for Geostationary High Resolution Ocean Applications (GEO-HR). Forward Model Description. Technical Report ESA Report GEOHR-D2 AO/1-7084/12/NL/AF (Version 1.1).

Lerebourg, C., Mazeran, C., Huot, J-P., Antoine, A. (2011) Vicarious adjustment of the MERIS Ocean Colour Radiometry. MERIS ATBD 2.24, Issue 1.0

Mayer, B. (2009). Radiative transfer in the cloudy atmosphere. EPJ Web of Conferences, 1:75–99.

Mayer, B. and Kylling, A. (2005). Technical note: The libradtran software package for radiative transfer calculations - description and examples of use. Atmospheric Chemistry and Physics, 7:1855–1877.

MERIS Level 2 Detailed Processing Model, June 2011, ref. PO-TN-MEL-GS-0006, Issue 8.0B available at http://earth.eo.esa.int/pcs/envisat/meris/documentation

Morel, A. (1988). Optical modeling of the upper ocean in relation to its biogenous matter content (case 1 water), Journal of Geophysical Research, 93, 10,749-10,768.

Morel, A., and S. Maritorena (2001). Bio-optical properties of oceanic waters: A reappraisal. Journal of Geophysical research, 106, 7763-7780

Morel, A., and B. Gentili (1996). Diffuse reflectance of oceanic waters. 3. Implication of bidirectionality for the remote-sensing problem. Applied Optics, 35, 4850-4862.

Morel, A. and Gentili, B. (1993). Diffuse reflectance of oceanic waters. ii bidirectional aspects. Applied Optics, 32(33):6864–6879.

Morel, A., Gentili, B., Chami, M., and J. Ras (2006) Bio-optical properties of high chlorophyll Case1 waters and of yellow-substance-dominated Case2 waters. Deep-Sea Res. I, 53, 1439-1559

Nicolas, J.-M., Deschamps, P.-Y., & Hagolle, O., 2006. Radiometric Calibration of the Visible and Near-Infrared Bands of Seviri Using Rayleigh Scattering and Sun-Glint Over Oceans, Proceedings of the 3rd MSG RAO Workshop (ESA SP-619). 15 June 2006, Helsinki, Finland. Editor: D. Danessy, p.19

Pope, R. M. and E. S. Fry, 1997, "Absorption spectrum (380-700 nm) of pure water. II. Integrating cavity measurements," Appl. Opt.,36, 8710-8723.

Shettle, E.P. and R.W. Fenn, 1979. Models for the aerosols of the lower atmosphere and the effects of humidity variations on their optical properties. Environmental Research Papers, AFGL-TR-79-0214, 20 September 1979, AFGL, Hanscom (Mass.).

Smith, R.C. and K.S. Baker, 1981, "Optical properties of the clearest natural waters (200-800 nm)," Appl. Opt.,20, 177-184.

Vermote, E., R. Santer, P.Y. Deschamps and M. Herman, In-flight Calibration of Large Field-of-View Sensors at Short Wavelengths using Rayleigh Scattering, Int. Journal of Remote Sensing, 13, No 18, 1992. http://www.tandf.co.uk/journals/tres

Yang, H. and Gordon, H. R. (1997). Remote sensing of ocean color: assessment of water-leaving radiance bidirectional effects on atmospheric diffuse transmittance. Applied Optics, 36(30):7887–7897.

Zagolski, F. (2010) Specification of the Contents of the MERIS Radiative Transfer Tools used to Generate the Level-2 Auxiliary Data Products. Doc PO-RS-PAR-GS-0003, issue 4.A

Závody, A. M., P. D. Watts, D. L. Smith, C. T. Mutlow, 1998. A Novel Method for Calibrating the ATSR-2 1.6-µm Channel Using Simultaneous Measurements Made in the 3.7-µm Channel in Sun Glint. J. Atmos. Oceanic Technol., 15, 1243–1252.

[End of Document]